Solar Wind Velocities at Comets C/2011 L4 Pan-STARRS and C/2013 R1 Lovejoy derived using a New Image Analysis Technique

Yudish Ramanjooloo, Geraint H. Jones

[1]Institute for Astronomy, University of Hawaii at Manoa, 2680 Woodlawn Drive, Honolulu, HI 96822, USA
[2]Mullard Space Science Laboratory, Department of Space & Climate Physics, University College London, Holmbury St. Mary, Dorking, Surrey RH5 6NT, UK
[3]The Centre for Planetary Sciences at UCL/Birkbeck, Gower Street, London WC1E 6BT, UK.

Key Points:

- Multi-point multi-latitudinal solar wind velocities can be derived from cometary ion tails.
- Images acquired from observatories, STEREO B provide comparable results to amateur astronomers.
- Results validated against 3D MHD models offer snapshots of the solar wind structure.

Corresponding author: Yudish Ramanjooloo, `yudish@hawaii.edu`

Corresponding author: Geraint H. Jones, `g.h.jones@ucl.ac.uk`

Abstract

The ion tails of bright comets have long been considered as natural tracers of the solar wind near these objects. Studies of comets and their ion tails allow inexpensive monitoring of key solar wind structures in the inner heliosphere, much of which is otherwise only accessible by in situ solar wind spacecraft measurements. Here, we present a novel technique to mine the rich archive of amateur, professional and spacecraft observations of cometary ion tails. To demonstrate this, we focus on Near-Sun comet C/2011 L4 (Pan-STARRS) during Carrington Rotations (CR) 2134 and 2135 and comet C/2013 R1 (Lovejoy) during CR 2118. We outline the technique's shortcomings, including its geometric limitations, and present a catalogue of radial solar wind velocities derived in the near-comet environment and information on the heliospheric conditions inferred from the measured solar wind. Complementary measurements, derived from folding ion rays and a velocity profile map built from consecutive images, are provided as an alternative means of quantifying the solar wind-cometary ionosphere interaction. We find that comets are generally good indicators of solar wind structure, but the quality of the results is strongly dependent on the observing geometry.

Plain Language Summary

Comets, as they move through the inner solar system, can be considered as natural laboratories of the solar wind. The solar wind is a continuous stream of fast charged particles that carries with it a remnant of the solar magnetic field into the solar system. Sourcing images from the internet and astrophotographers, we developed a new technique and the software to measure the solar wind speed in the comet's orbital plane by using the ion tails of comets. The ion tail behaves similarly to a transparent windsock and indicates the direction of the solar wind. This allowed us to create a snapshot map of the solar wind variations along a comet's orbit when it is close to the Sun. We also outline the reliability and the limitations of the technique and a catalog of solar wind velocities from comets C/2011 L4 (Pan-STARRS) and C/2013 R1 (Lovejoy). We find that with the right geometry, comets are good and efficient probes of the solar wind. This catalog of speeds will help us better understand the three-dimensional structure and variability of the solar wind.

1 Introduction

The cometary ion tail is an induced magnetotail structure, pointing approximately along the anti-sunward direction but lagging the true anti-solar direction by a few degrees. This aberration angle arises from a combination of the comet's orbital velocity and the local solar wind velocity, v_{sw}. With a favourable observing geometry, comets with a suitably bright ion tail, can contribute towards increasing our understanding of the variability in v_{sw}.

The first hints of the solar wind's existence came from observations of comets' ion tails (Hoffmeister, 1943; Biermann, 1957). Few spacecraft have been launched specifically to probe the solar wind in situ. At the time of writing, Parker solar probe and Solar Orbiter are the two most recent spacecraft to probe the solar wind close to the Sun. In situ measurements are limited to predetermined spacecraft trajectories which are confined to close to the ecliptic plane - Ulysses being the exception by conducting three near pole-to-pole heliolatitudinal scans of the solar wind - whilst comets have a range of trajectories and sample a wide range of helio-longitudes and latitudes (Jones et al., 2018).

J. Brandt and Chapman (2004) encapsulated the benefit of heliospheric research by presenting the following paradigm for non-solar maximum conditions:

1. Smooth, fast high latitude solar wind lead to largely featureless ion tails at these latitudes, and
2. Slower and more variable streamer belt flow nearer the solar equator are associated with highly dynamical and structured ion tails for comets in this region (Figure 1).

Measurements of comets' ion tail orientations have long been used to successfully constrain the local v_{sw} in studies such as Belton and Brandt (1966); J. C. Brandt (1967); Brandt, Roosen, and Harrington (1972); Brandt, Harrington, and Roosen (1973); Jockers (1981, 1985), and Buffington et al. (2008). These remote observations of the continuously varying morphology, dynamics, and orientations of a comet's ion (Type I) tail have also yielded extensive information on the large-scale solar wind structure at the comets.

Ion tail disconnection events (DEs) are considered to be key markers of solar wind phenomena. DEs could be due to variation in ion production rates, increase in solar wind pressure, or most likely in the majority of cases, magnetic reconnection. Niedner and Brandt (1978) associated tail disconnections with crossings of the heliospheric current sheet (HCS). However, it should be noted that Delva, Schwingenschuh, Niedner, and Gringauz (1991) found a correlation between sector boundaries and ion tail disconnections in only 50% of the considered events. They further determined a connection between large tail events and density enhancements in the solar wind.

Encounters with coronal mass ejections (CME) can lead to rapid reconfigurations of tail features and their orientations (Jones & Brandt, 2004). Vourlidas et al. (2007) linked the first reported observation of an Interplanetary Coronal Mass Ejection (ICME)-ion tail interaction where the ICME was also visible, which led to a disconnection of comet 2P/Encke's ion tail. Locations of co-rotating interaction regions (CIRs), where fast and slow solar wind regions interact, and transitions between different solar wind regimes can be accurately identified from kinks in the ion tail, i.e. large and rapid changes in the aberration angle.

The source surface, $\sim$2 to 2.5 $R_{\odot}$ from the Sun, is the hypothetical boundary beyond which the magnetic field and the plasma flow is assumed to become purely radial. Departures from flow radiality can occur within transient interplanetary solar wind phenomena such as CIRs and ICMEs or when the solar wind encounters a magnetospheric obstruction. These interactions cause a deflection of the bulk radial plasma outflow at the stream interface or at the ICME's leading edge and introduce an azimuthal and/or meridional (north-south) component (Richardson et al., 1996; Jones, 2002; Owens & Cargill, 2004).

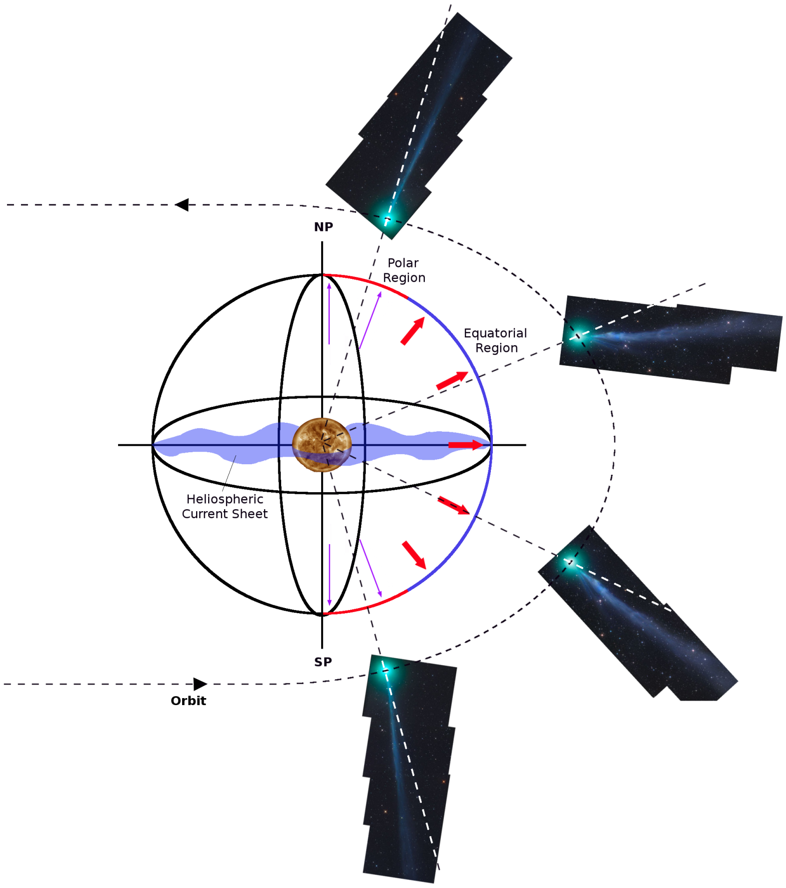

99 **Figure 1.** Illustration of comet-solar wind paradigm (Adapted from Brandt and Snow (2000). Smooth, fast solar wind flow at high solar latitudes lead to largely featureless ion tails. Comets in the solar equatorial region encounter slower and more variable streamer belt flow which have been associated with highly dynamical and variable ion tails which can contain both large-scale and fine structures. Image credit: Courtesy of Gerald Rhemann and NASA/SDO and the AIA, EVE, and HMI science teams.)

We will introduce our new technique and software that converts cometary ion tail images into multi-point multi-latitudinal solar wind speed estimates. A complementary software package further offers dynamical feature tracking in consecutive images, which is used in the analysis of transient phenomena associated events in the ion tail, and tail ray folding periods. Our technique makes use of images that have been extrapolated along the line of sight of the observer and mapped onto the comet's orbital plane.

2 Data Sources and Instrumentation

We analyzed the tails of two comets: C/2013 R1 (Lovejoy) during Carrington Rotations (CR) 2118 and Near-Sun comet C/2011 L4 (Pan-STARRS) during CR 2134 and 2135. The observing geometry of these two comets highlight the value of this technique to determine catalogues of radial solar wind velocities in the near-comet environment. They also offer contrasting examples of the limitations we face due to viewing geometry.

We used images of C/2013 R1 (Lovejoy), taken both by amateur astronomers using consumer-grade equipment, and professional observations using the 2.5-metre Isaac Newton Telescope, and images of C/2011 L4 (Pan-STARRS), from the STEREO-B spacecraft. These data were used to develop the technique and software to extract multiple estimates of the local radial solar wind velocity, which we refer to as v_{sw_r}. These comets were chosen based on their visual brightness, orbit geometry and the extensive online collection of amateur and professional images. They strongly demonstrate the usefulness and reliability of this technique.

2.1 Non-professional images

The advent of highly sensitive commercial CCD and CMOS sensors, coupled with modern telescopes with large fields of view (FOV) has led to the quality of modern comet images being often better than that of professional photographs from a few decades ago. High quality contributions from a globally distributed network of comet enthusiasts hold the potential for near-continuous monitoring of comets.

Astronomical images acquired by non-professionals were sourced from numerous online repositories available via media platforms (e.g. Google, Astrobin, Flickr). Internet-sourced images lacked conformity in terms of image format, FOV, image size and calibrations. Often, the images were without precise timing or geographic information. This is in agreement with observations by Lang and Hogg (2012), who found that only ~70% of the meta-data supplied by amateur astrophotographers was correct.

2.2 Isaac Newton Telescope / Wide-Field Camera

The Isaac Newton Telescope (INT) is a 2.5m optical telescope located at the Roque de los Muchachos, La Palma, Spain. The facility's Wide Field Camera (WFC) is a 4 CCD mosaic covering a 34 x 34 field of view with a chip gap of ~ 0.5'. Each CCD pixel corresponds to 0.33" on sky. Author YR along with K. Birkett, used the WFC to observe comet C/2013 R1 (Lovejoy) using standard broadband photometric filters Sloan r and Harris B (York et al., 2000) from 2014 January 2 to 6.

2.3 STEREO B

The Sun Earth Connection Coronal and Heliospheric Investigation (SECCHI) (Howard et al., 2008) instrument consisting of 2 coronagraphs (COR1 and COR2) and a pair of heliospheric white-light imagers (HI1 and HI2) aboard the STEREO B spacecraft (Kaiser, 2005) were used to estimate v_{sw_r} at C/2011 L4 (Pan-STARRS). The HI1 and HI2 imagers provide a 20° and 70° FOV around the Sun-Earth line along the ecliptic and are centered off the solar center by 14° and 53°.7 (Eyles et al., 2009), looking at solar elongations from ~3° to 23°.5 (~12 - 92 $R_\odot$) and 20° to 90° (~ 73 - 318 $R_\odot$) respectively.

2.4 CME catalogue

The CME catalogue used here is generated and maintained at the CDAW Data Center by NASA and The Catholic University of America in cooperation with the Naval Research Laboratory (Gopalswamy et al., 2009). The catalogue lists all transient ICME events from the SOHO LASCO C2 and C3 coronagraphs (Brueckner et al., 1995). The central position angle (CPA) can be useful in distinguishing between simultaneously occurring ICMEs. This is measured counter-clockwise from solar north in degrees. Once the ICME expansion stabilises in the C2 FOV, a sky-plane width is measured, when possible. Infrequently, certain ICMEs will exhibit significant acceleration or deceleration, thus reducing the linear speed to merely a guide of the average ICME speed within the LASCO FOV. Combining the date and time of ICME eruption, its linear plane-of-sky speed, width and CPA with the heliocentric distance of our comet and the angle with the solar north pole, we can constrain a list of ICME candidates likely to encounter the comet for a given date.

3 Technique

An ion tail is always generally oriented in the anti-sunward direction; however it always lags the true anti-solar direction by a few degrees, opposing the direction of the comets motion. It is well established that solar wind conditions control and maintain the appearance of the ion tail and that the tail axis is a composite vector of the v_{sw} vector and the comet's orbital motion. An extended ion tail records a time history of solar wind changes over several hours.

Remote observations of the ion tail are a potentially invaluable resource to probe the high spatial variations of solar wind structures across a wide range of heliospheric latitudes and distances and over long timescales. We have developed a novel system of extracting valid local v_{sw_r} estimates, as well as characterising local parameters for transient interplanetary events near comets, allowing us to use comets as solar wind monitors within the inner heliosphere. To demonstrate this technique, we investigate amateur images of bright comets with a small geocentric distance and good observing geometry from Earth. By employing v_{sw_r} measurements from amateur and professionally acquired images, we demonstrate that comet observations can provide reliable estimates of the ambient local v_{sw} at the comet and can lead to the identification of the local parameters of coronal mass ejections (CMEs), the locations of heliospheric current sheet (HCS) crossings, as well as the locations of co-rotating interaction regions (CIRs) during periods of quiescent solar activity.

When the projected observing geometry is good, i.e. when the angle between the Sun, target and the observer (S-T-O angle) is close to 90°, and that the observer is well outside the comets orbital plane, i.e. at a "large enough" orbit plane angle, we can constrain the v_{sw} (Figure 2). The ideal geometry for comet observations from Earth would occur when the S-T-O angle and orbit plane angle are both near 90°.

The dynamical variations of and plasma density distribution along the tail are controlled by the mass-loading process. Ever-changing, extensive features in the tail such as condensation knots and kinks generally indicate the flow state of the solar wind, whether the comet is surrounded by quiescent fast solar wind or traversing a more variable solar wind flow. Kinks in the tail are often clues that the comet may be moving from one solar wind regime to another.

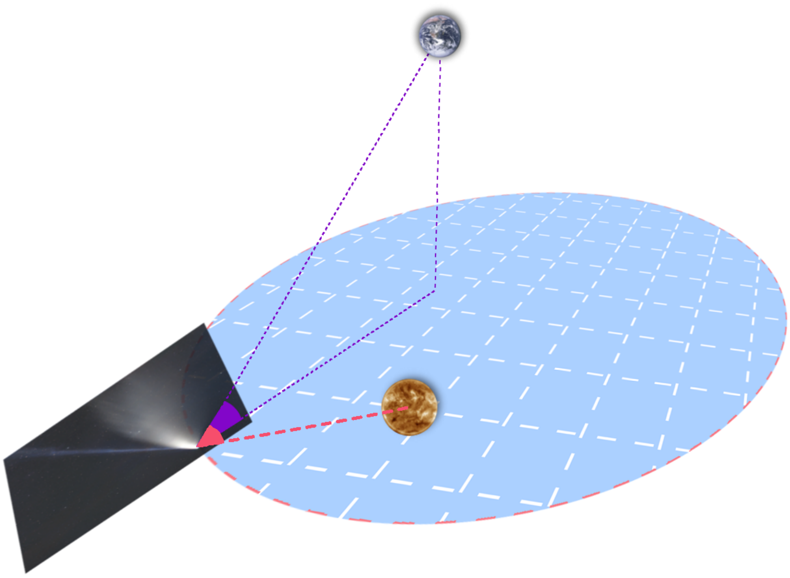

Figure 2. The orbit plane angle is the angle (purple) between the line of sight from the observer to the comet and the comet's orbital plane. The Sun-Target-Observer (S-T-O) angle is given in red. Image credit: Gerald Rhemann (Comet C/2020 F3 (NEOWISE)); SDO (Sun); NASA Apollo (Earth).

3.1 Deriving Solar Wind Velocities

The ion tail orientation can be exploited to pin down an approximation of the local radial flow of the solar wind (SW). The aberration angle, ϵ, is defined as the angle between two vectors: the composite vector of the comet's heliocentric orbital motion vector and the solar wind velocity vector, and the prolonged radius vector from the sun, i.e. the radial flow of the solar wind [Figure 3a].

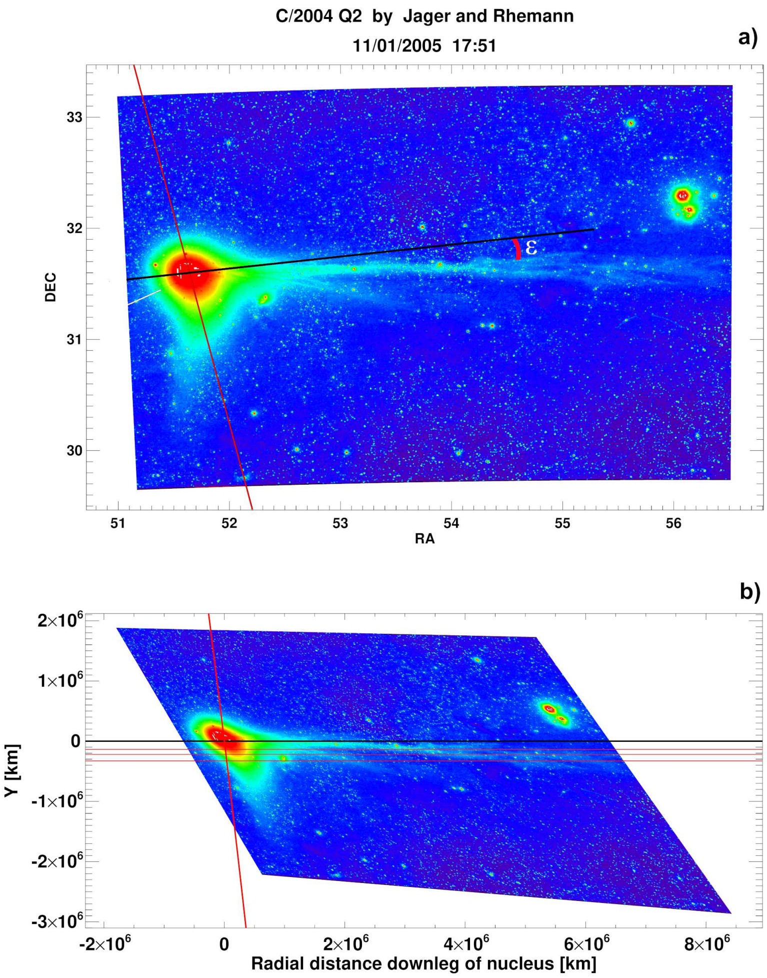

Figure 3. Comet C/2004 Q2 mapped in (a) celestial coordinates and (b) cometocentric coordinates. The orbit (red), the extended solar radial vector (black) and the aberration angle (red angle) are labeled in (a). In (b), the image has been transformed so as to keep the sun-comet line fixed with the predicted comet nucleus location as the origin. The horizontal sun-comet line (black) in the second image is the extended radial vector from the sun. The comet's orbit is the red vertical line. The horizontal red lines are extended solar radial vectors originating from where the comet's nucleus would have been at that time. These radial vector cross-sections of the ion tail provide an indication of the distance travelled by each plasma bundle from the comet's orbit to the ion tail.

Figure 3 illustrates the slight difference between the two techniques of determining the solar wind velocities, using a non-study comet as an example. The first technique uses the aberration angle to determine the solar wind velocity. The second technique is the technique we will present in this paper. The orientation of the ion tail arises from the combination of the comet's orbital velocity and the local solar wind velocity (Hoffmeister, 1943; Biermann, 1957). The composite vector equation is given by:

$$\overline{T} = \overline{V} - \overline{U} \tag{1}$$

$\overline{T}$ is the apparent axial vector of the ion tail, $\overline{V}$ is the solar wind velocity vector and $\overline{U}$ is the comet's orbital velocity vector. In the top image, it is possible to measure the aberration angle of the ion tail on the plane of the sky. By projecting these vectors onto the comet's orbital plane, as described in Konopleva and Rozenbush (1974), an expression for the aberration angle can be defined. The $\overline{V}$ vector can in principle be resolved into its radial (V_r) and tangential (V_ϕ) components. However, this is challenging as a larger tangential component cannot always be uniquely separated from a radial solar wind speed change. Rearranging the equation for V_r, we obtain:

$$V_r = \frac{U \sin\gamma - V_\phi \cos i}{\tan\epsilon} + U \cos\gamma \tag{2}$$

γ is defined as the angle between the extended radial vector of the comet and the vector of the comet's orbital velocity, i is the inclination of the comet's orbital plane to the solar equator and ϵ is the aberration angle.

In our technique, the images are instead extrapolated along the line-of-sight of the observer and mapped onto the comet's orbital plane; the solar wind flow is assumed to be purely radial. Once the image is mapped onto the comet's orbit a simplified geometry of the system can be extracted. The aberration angle ϵ can thus be simplified to the equation below, where $U_\perp$ is the perpendicular component of the comet's velocity to the prolonged radius vector and V_r is the radial solar wind velocity. The radial component of the orbital velocity, and the non-radial components of the solar wind are both assumed to be negligible here.

$$\tan\epsilon = \frac{U_\perp}{V_r} \tag{3}$$

The bottom image in Figure 3 encapsulates the adopted sampling method. With cometocentric distances calculated for the image, multiple cuts, shown in red, are taken parallel to the radial vector with set time steps. Solar wind velocities are then calculated from these known quantities. Since each image is projected onto the comet's orbital plane, the best framework to estimate the local solar wind radial velocity, which we now refer to as v_{sw_r} for the demonstration of our technique. All the previous considerations ($\overline{U}$, i and γ) are factored in within the projection mapping. We also computed V_r using the simplified equation for the aberration angle. They both produced solar wind velocities within the same range, with some erroneous values produced for very small aberration angles, for instances where the ion tail lies close to the extended radial vector. Even under excellent geometrical conditions, without mapping the image onto the comet's orbital plane, precisely measuring the aberration angle can be difficult as the comet's orbital velocity is generally an order of magnitude smaller than the solar wind velocity (J. C. Brandt & Heise, 1970).

3.2 Developing the Software

The pointing, field of view, plate scale and orientation of comet images are essential in order to derive estimates of the solar wind conditions in a comet's vicinity. These are frequently unknown for amateur observations. Using Astrometry.net source code V0.50 (Lang et al., 2010) has greatly simplified the acquisition of this information, by returning the requisite information almost instantaneously. This robust astronomical image solver computes the equatorial celestial coordinates of each pixel in the original comet images. Hogg and Lang (2008) reported the success rate of Astrometry.net to be >99.9 % for contemporary near-ultraviolet and visual imaging survey data, with no false positives.

Each comet's ephemeris was downloaded from JPL Horizons (Giorgini et al., 1996) in the geocentric equatorial and heliocentric ecliptic coordinate systems (epoch J2000.0). The heliocentric coordinates of the observer's orbit (for this study, the geocenter or STEREO spacecraft) are also downloaded.

The ground-based observations used here were obtained from locations all around the globe. It is not always obvious which time zones were used when the images are made available in online repositories. Moreover, the timing metadata, when provided, was not always accurate nor precise. As an accurate astrometric solution was obtained for the images, an approximate observing time was independently deduced from the comets orbit; this helped to identify and correct erroneous times. We estimate the percentage of successful solves through this procedure to be >95% after processing over 500 images. Once a time and date of observation for the image has been estimated, each image was converted from celestial coordinates to heliocentric ecliptic longitudes and latitudes, and then to heliocentric ecliptic Cartesian coordinates, as described below.

From the ascending node and inclination of the comet's orbital plane (Figure 4), we define the normal of the comet's orbital plane, $\overline{O}$. The image and orbit coordinates are converted to ecliptic Cartesian coordinates. The magnitude of the vector to each pixel from Earth, l, is computed from the position of Earth at the time of image exposure and the normal to the comet's orbital plane (Equation 4). Each pixel vector is translated to a new frame of reference using the Sun as origin and accounting for light-travel time.

$$l = \frac{\overline{O}.\overline{E}}{\overline{O}.\overline{P}} \tag{4}$$

l is the scalar length of the vector of each pixel in the image from Earth. The magnitudes of $\overline{O}$ and $\overline{P}$ are unknown, so a unit vector is assumed for both. $\overline{P}$ is the unit vector to each image pixel from Earth and $\overline{E}$ is the vector from the Sun to the Earth.

The final section of the software computes the vector product of the perihelion vector and the vector perpendicular to the comet's orbital plane to define the x and z axes of a new coordinate system based on the comet's orbital plane. Every object in the previous system is mapped with respect to the comet's plane. The multiple transformations are needed as the comet's orbital plane provides the best framework for estimating v_{sw}.

Each individual image is plotted with its comet's "nucleus" defined as the origin of the frame of reference and the comet's orbit is rotated so that the Sun is always to the left of the image, and the Sun-nucleus line is horizontal. Note that the optocenter (optical center) is not necessarily the true location of the nucleus. The brightness of the coma and only having access to post-processed images online often make it impossible to resolve the comet's nucleus via direct imaging of the comet from Earth. The radius vector from the Sun to the 'nucleus' is extended across the image and defines the x-axis. The z-axis is defined as the normal to the comet's orbital plane.

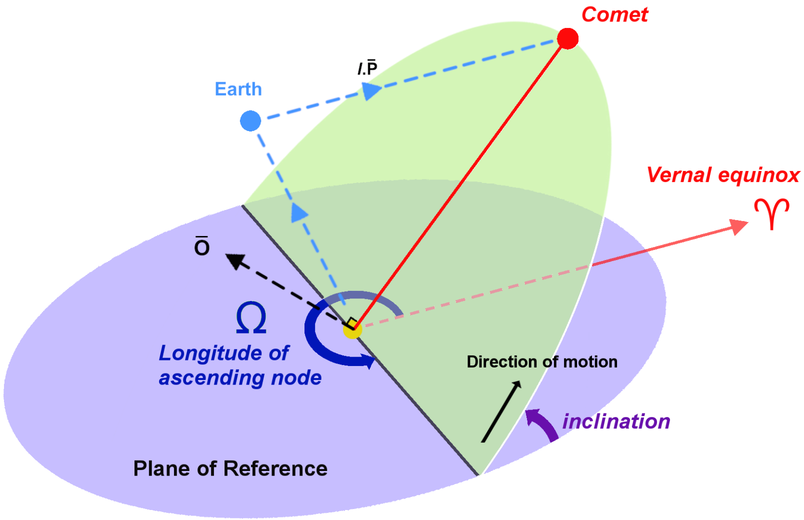

Figure 4. Schematic of the longitude of ascending node and inclination required to calculate the normal to the comet's orbital plane. The plane of reference is the ecliptic.

The ion tail center at any position lagging the comet's orbit is set as the point where the extended radial vector intersects the ion tail. Assuming that the solar wind is always flowing radially, the center of the tail downstream of any position along the orbit that the nucleus has already passed, provides the v_{sw_r} when the comet was at that orbit location. Rather than regarding the ion tail as a continuous flow of material, for the benefit of simplification of the necessary coding, we instead consider the tail as a set of numerous discrete plasma "packets" flowing radially away from the Sun at the local v_{sw}. By taking multiple cross-sections across the ion tail along the radial anti-sunward direction, we extract multiple velocities across the image along the extended radial vector from the Sun.

We could not automate identification of the ion tail center due to the low relative surface brightness of the tail with respect to the surrounding sky background. An interactive colour stretching function with a Graphical User Interface (GUI) was incorporated into the software. The user can define and store a new colour palette for each image to accentuate features of interest. The user then selects the area intersecting the extended radial vector and the ion tail (where the red radial vector overlaps the ion tail in Figure 3), from which a tail center and an uncertainty of $\pm 1/6$ of the ion tail coincident with the radial vector were determined. Measurements of the tail center were generally taken from 1×10^6 km onwards, as the edges of the ion tail closest to the nucleus merge with light from the coma and dust tail, making the various components difficult to separate. The local v_{sw_r} is estimated from the distance travelled by the plasma packet, from the position where it left the comets orbit to the ion tail center, divided by the time difference between the comet's current position in the image and its position when the plasma packet left the vicinity of the comet 'nucleus'.

3.2.1 Tracking Fast Moving Sub-structures

An alternative method of quantifying the v_{sw} is to visually track dominant features in consecutive images. These include identifiable kinks, condensation knots or disconnections. Flow vector maps (hereafter vector maps) are not new in the study of cometary features (e.g. Rauer and Jockers (1990); Yagi et al. (2015)). The criteria employed for the collection of amateur data for this purpose is that the images had to be observed during the same observing night, regardless of location, and with an adequate time separation in between to ensure that we are looking at the same evolving structure and to compensate slightly for errors in the image time.

3.2.2 Tracking of Tail Rays

Tail rays, or tail streamers when within the main ion tail, form much of the fine-scale structure of the ion tail. Typical tail ray lengths are on the order of $\sim 10^6$ km (Minami & White, 1986) with radii $\sim$ 2000 to 4000 km (J. Brandt & Chapman, 2004). Consecutive photographic evidence of tail rays folding around the main tail axis suggests that the ionised plasma can be considered as magnetic tracers of the Heliospheric Magnetic Field (HMF) as it drapes around the comets nucleus (Moore, 1991; Watanabe, 1991).

To study the motion of features, we overlaid consecutive images and measured the radial velocity shear across the tail ray as it folded. We assumed a simple model of symmetrical pairs of folding rays acting as tracers of the mass-loaded draped HMF and that measurements of the rays' angular closing rates can reliably constrain the velocity of the mass-loaded solar wind. If multiple rays were visible in consecutive images, we derived an acceleration of the v_{sw} near the comet head. We expect that as the tail rays curve and lengthen, as they merge with existing plasma along the main tail axis, measurements taken near the nucleus will yield slower velocities than further down the tail streamer. This technique is limited to the region close to the nucleus, $\sim 1\times10^5$ - 1×10^6 km and requires an adequate spatial and temporal resolution.

In contrast to previous studies, we did not calculate the angular closing rates of the tail rays. Schlosser (1967) reported 120-170 kms^{-1} for comet C/1908 R1 (Morehouse). Watanabe (1991) measured the mass-loaded solar wind and reported 20% lower velocity for comet 23P/Brorsen-Metcalf than v_{sw} derived by radio scintillation. Moore (1991) developed a fairly similar technique to ours but did not project the images onto the plane of the sky at the comet. The tail rays were then measured as they folded about the main tail axis, though no attempts were made at producing a v_{sw}. It can be argued that Moore's approach is safer, since we do not know of any evidence showing that the tail rays are constrained to the comet's orbital plane.

3.2.3 Uncertainties

The vector map technique suffered from imprecise astrometric mapping. Due to large optocenters, times derived via our software will be slightly limited in precision. The relatively high velocities of the bulk solar wind and the large FOVs of most images drowned out the timing uncertainty. For the vector maps and tail ray methods, when two consecutive images are considered from different observers, and for small FOVs, this effect becomes considerable as the timing uncertainty will be compounded and cannot be knowingly accounted for. The feature-tracking velocities are calculated from $\Delta r/\Delta t$, where Δr is the distance that the feature has travelled between subsequent images and Δt is the time difference between the two. The error is given by:

$$\frac{\sigma_{feature}}{|v_{feature}|} = \sqrt{\left(\frac{\sigma_r}{r}\right)^2 + \left(\frac{\sigma_t}{t}\right)^2} \tag{5}$$

For the feature tracking, the features were composed of a series of expanding amorphous blobs of varying shapes and sizes and their location is measured by a single position estimated as the features center. The error is assumed to be the distance error of the projected pixel vector. The same process was adopted for the tail rays. The error on Δt is given by:

$$\sigma_t = \sqrt{\sigma_{t_1}^2 + \sigma_{t_2}^2} \tag{6}$$

The distance error between feature motions in consecutive images can be simplified to the equation below, where σ_x and σ_y are the pixel distance errors:

$$\sigma_r = \sqrt{\sigma^2_{\Delta x} + \sigma^2_{\Delta y}} \tag{7}$$

where

$$\sigma^2_{\Delta x/y} = \sigma^2_{x/y1} + \sigma^2_{x/y2} \tag{8}$$

Vector map analysis was performed on both comet whereas the folding tail rays methodology was only applied to C/2013 R1 for both the amateur and INT observations. A full treatment of the uncertainties is available in the online supporting information.

3.2.4 Orbit Plane Angle & Non-Radial Flows

The orbit plane angle, an important consideration in the comet-Sun-Earth geometry, is the angle between the line of sight from the observer (at Earth) to the comet, and the latter's orbital plane (Figure 2). A non-zero value indicates that the observer is viewing from a position that is not in the comet's orbital plane. The ideal geometry is when the orbit plane angle is near 90° and the observer is sufficiently far from the comet's orbital plane. Deviations from the ideal geometry will result in an over/under-estimation of the ion tail's true location, which will be dependent solely on the magnitude of the angle and whether the observer is leading or lagging the comet's motion.

The orbit plane angle is equal to zero every 6 months, as the Earth crosses the comets orbital plane. When the orbit plane angle nears zero, images taken during this period become stretched excessively when mapped onto the comet's orbital plane. The projection mapping technique is a strong function of the orbit plane angle and the distance between the observer and the comet. Extreme scenarios when the observer is far from the comet and the orbit plane angle is low, the pixel vector extrapolation breaks down and results in extremely lengthy vectors stretching out in all directions. Thus, any radial estimates derived from these images would be unreliable and unrealistic. However, we can sometimes resolve the images by zooming in on where the comet's orbit and the Sun-comet line intersect. Figure 5 clearly shows that the mapping technique can sometimes still provide usable results even under these geometric conditions. Images taken during this time period will be recording deviations of the comet along the z-direction, i.e. out of the comet's orbital plane. This provides the opportunity to measure the deviation angle of the comet's ion tail from its orbital plane due to the non-radial flow of the solar wind. Only a small proportion of images can be used for this as demonstrated in **section 4.1.1**.

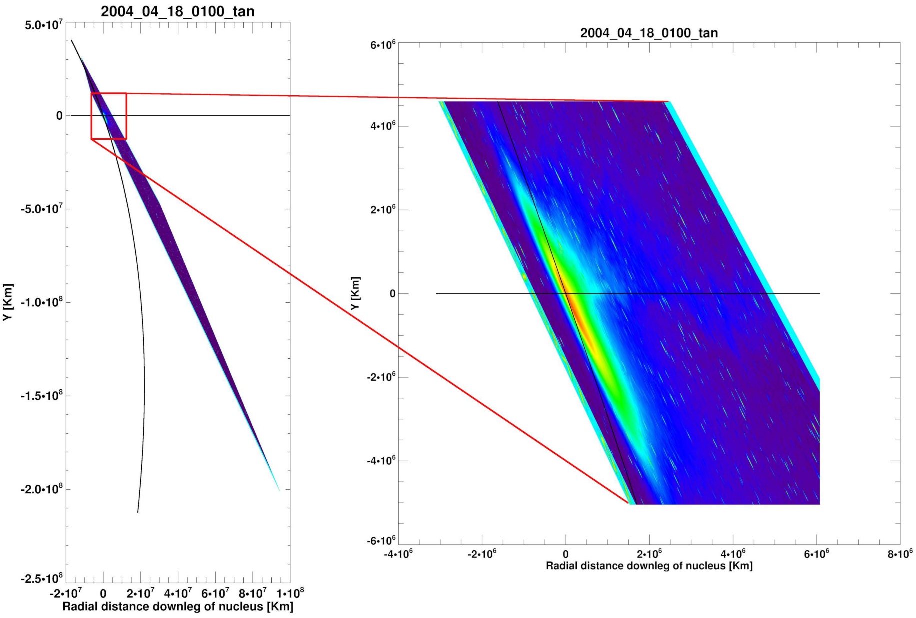

Figure 5. An example of extreme image distortion at low orbit plane angles: A mapped image of comet C/2001 Q4 NEAT taken on 2004 April 18, shortly before the orbit plane angle reached $\sim 0°$ on 2004 April 20. The horizontal line at y=0 is the extended Sun-comet line. The black curved line is the comet's orbit in this reference frame. The image on the right is a close-up of the coma and shows a very faint ion tail in blue close to the radial vector and the sky background in purple. Image credit: Loke Kun Tan

3.2.5 Mercator Map

The heliocentric coordinates of each notional plasma packet that reached the comet of interest can be ballistically traced back to its assumed origin at the solar wind source surface. Its cometocentric coordinates are first converted back into heliographic spherical coordinates (Carrington rotation system). Using the mean sidereal Carrington rotation rate of the sun, we map the plasma back to its source longitudes for possible slow (400 kms^{-1}) and fast (800 kms^{-1}) approximate speeds at which it left the solar wind source surface. We assumed typical slow and fast v_{sw} without knowing the true values, and that they remain at this same speed on their path from the Sun to the comet.

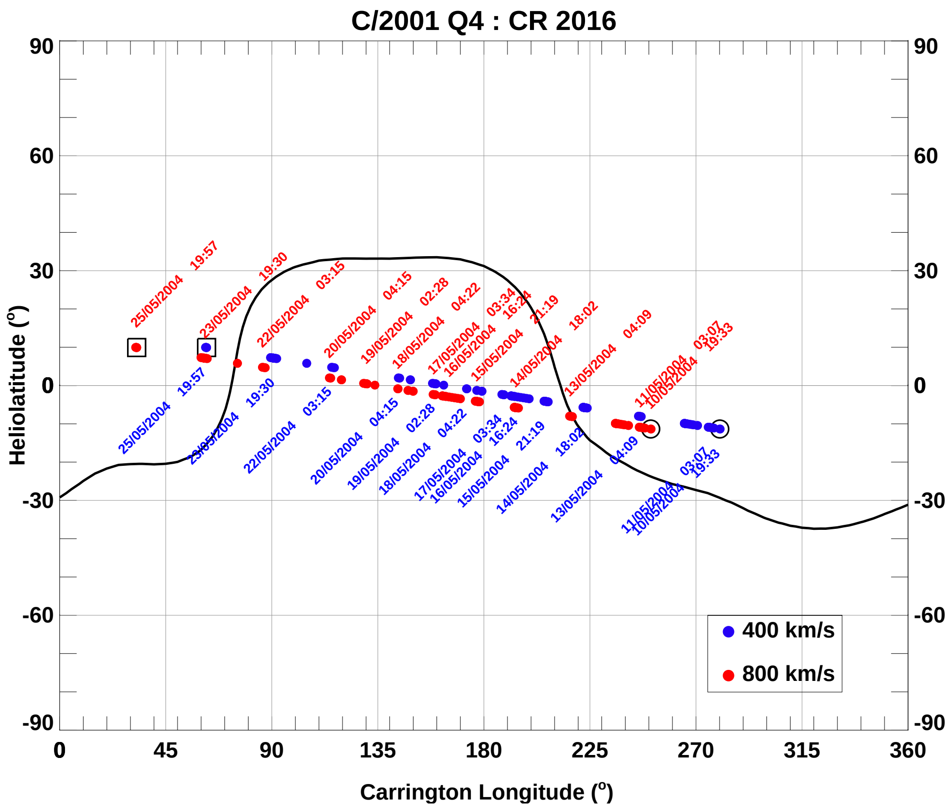

Figure 6. An example of a Mercator map of the solar wind source surface for Carrington rotation 2016, showing the computed source locations of solar wind packets that reached comet C/2001 Q4 (NEAT). Estimates assuming slow wind (400 kms^{-1}) are in blue and fast solar wind (800 kms^{-1}) sources are in red (800 kms^{-1}). See text for further details.

Figure 6 shows the sources for the notional slow and fast solar wind. Only the first date and time for a range of plasma packets are plotted for each day. Data points within the black circle represent the first date sampled for this Carrington rotation and the last data points are enclosed by a black square.

The black solid line is the approximate position of the neutral line on the solar wind source surface as calculated by the Wilcox Solar Observatory research team (Schatten et al., 1969; Altschuler & Newkirk, 1969; Hoeksema et al., 1991). This is a reasonable first-order proxy for the heliospheric current sheet's location. We traced back our measurements to the 2.5 $R_\odot$ radial solution from the Wilcox observatory.

3.3 Integration of SOLARSOFT

High-quality difference images of comet C/2011 L4 (Pan-STARRS) highlighted fainter substructures in the ion tail than our current methodology and were used to produce higher resolution v_{sw_r} from the images. The Solarsoft package (`http://sohowww.nascom.nasa.gov/solarsoft/`), recommended for the data reduction and analysis of the suite of solar instruments available, was integrated to work seamlessly with our software, with both level 1 and 2 (L1 and L2) data from the STEREO Heliospheric Imagers and level 0.5 and level 1 (L0.5 and L1) data from the SOHO LASCO coronagraphs. SOHO L1 data incorporates corrections to photometric calibrations, vignetting, geometric distortion effects and suppressing stray light (Morrill et al., 2006). STEREO L0 data are the raw, uncalibrated data and L1 contain flat-fielding, alignment and shutterless corrections to the L0 data. L2 data includes the removal of the dust component of the corona – the F corona (Koutchmy & Lamy, 1985) – and is therefore ideal for use. The HI-1 frames are usually 30 minutes worth of exposures, stacked with 40 minute cadences. The error on the observing time is thus taken to be ± 15 mins.

3.4 Data Rejection

The primary reasons for rejecting images were as follows:

- Image was of poor quality, e.g. star trails, saturated image or incorrect astrometric solutions
- Ion tail was too faint to resolve or its edges are poorly defined against the sky background
- The image FOV was too large to resolve ion tail
- In certain instances, the first v_{sw_r} measurement was discarded. The proximity of the ion tail to the coma made determining the tail center unreliable
- Inaccurate image mapping due to $\sim 0°$ orbit plane angle

4 Results

4.1 C/2013 R1 (Lovejoy)

The brightness of comet C/2013 R1 (Lovejoy), discovered on 2013 September 7, peaked in brightness at m_v about +4.5 around perihelion (T = 2013 December 22), where its solar elongation was 51°. Its visual magnitude remained between +4 and +6 during most of the observations, according to Yoshida Seiichi's lightcurve of amateur observations (`http://www.aerith.net/index.html`).

Only observations ± 2 weeks around its perihelion were analysed (Ramanjooloo & Jones, 2021b). The set of amateur images were mapped onto the comet's orbital plane with the y-axis defined as the direction to the comet's perihelion (Figure 7). The comet's orbital plane was inclined by 64°.0. Amateur images of C/2013 R1 from this period allowed us to probe the inner solar system to intermediate heliographic latitudes from 34°.0 to 54°.0. We obtained 109 v_{sw_r} estimates from 36 fully processed images out of 123 amateur images with a detectable ion tail. 7 solar wind estimates did not pass the rejection process and 43 of the remainder are measurements of a sinuous and variable ion tail that were too challenging to interpret with sufficient confidence. The amateur images amassed for this time period were supplemented by our own observations undertaken at the Isaac Newton Telescope in January 2014, presenting a unique opportunity to validate the quality of amateur images using high quality observations from an established scientific observing facility. The comet was at high heliographic latitudes during the INT observations (∼60°).

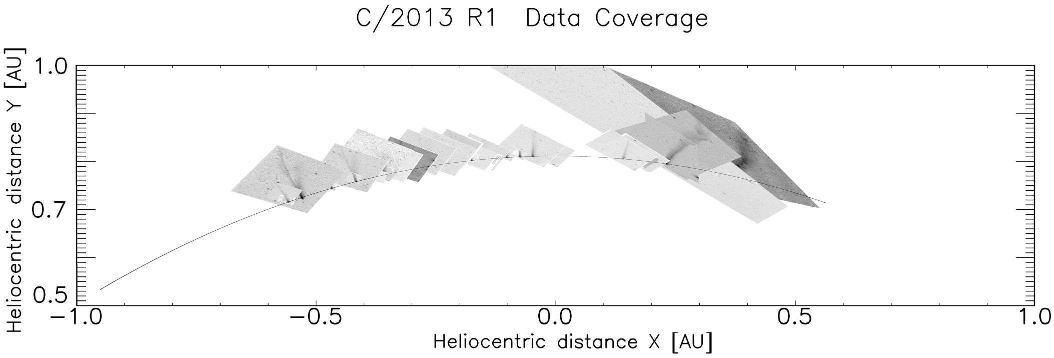

Figure 7. Data coverage for C/2013 R1 (Lovejoy). Only the amateur images have been mapped. The Sun is at the origin of the coordinates, and the Y-axis is defined as the direction to perihelion. Earliest image is to the right, increasing chronologically towards the left.

INT observations were undertaken from 2014 January 02 to 07, when the comet was at a heliocentric distance of ~0.85 AU and 1.15 AU from Earth. C/2013 R1 was a morning target, limiting observations to 40-60 minutes. A full list of observations and why they were rejected can be found in author YR's thesis (Ramanjooloo, 2015). Each image consists of 4 CCD frames. The images were post-processed through a coaddition, dust subtraction and contrast enhancement pipeline. The result was a set of 11 images showing intricate details of the ion tail's fine structure and the region close to the nucleus. A total of 28 radial velocity estimates were extracted. 19 of these were measured from a dynamic and variable ion tail.

The brightening sky during twilight proved to be a major noise source. For the last few images taken during each night, the signal-to-noise ratio (SNR) was too low to resolve the ion tail. By subtracting the sky contribution from the r filter images, we were able to extract difference images with multiple tail rays and an ion tail fanning out, even in the twilight images. Where feasible, the images were stitched together to create larger mosaics of the coma and ion tail (Figure 8). Multiple pointings were required to image the entire tail. It is important to note that in the time taken for the exposure, image read out and telescope slew, there was a small angular and positional error between the sections of the ion tail observed due to time elapsed. If the total time between two consecutive images was 2-3 minutes, this was enough time for the tail dynamics to have also evolved slightly, such that a mosaic of the two images will not be entirely concurrent snapshot. A list of the observations undertaken is given in the online supporting information.

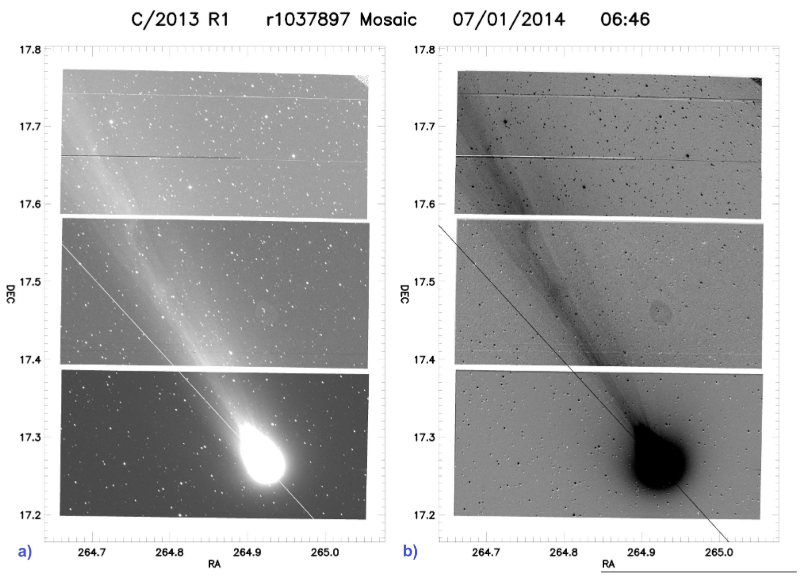

Figure 8. A coadded Harris B filter image of C/2013 R1 (a) and a dust-subtracted difference image (b) from a pair of coadded Harris B and Sloan r images. The comet's orbit is the straight line overlaid in the images. Observations were undertaken by K. Birkett and Y. Ramanjooloo on 2014 January 07.

Coadded images were constructed from B and r images taken close to each other in time and reduced using usual flatfielding techniques to minimise motion blur. Due to short exposure times and the limited number of images in a group, the end results were insensitive to large motion blurs. Figure 8a shows the original coadded CCD images and Figure 8b shows the image following dust continuum subtraction (Wilson et al., 1998). To account for the different pixel locations of the nucleus, each coadded image in a set of difference images was warped using the astrometric parameters of the reference image before mapping onto the comet's orbital plane (Figure 9).

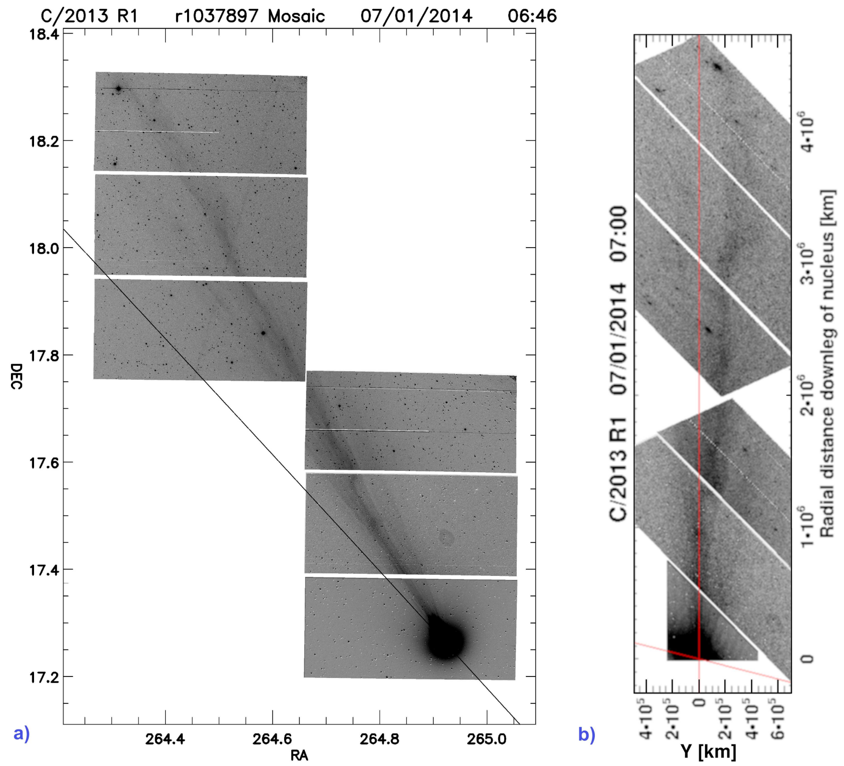

Figure 9. Stacked, dust subtracted mosaic image of C/2013 R1 in celestial equatorial coordinates (a), with the comet's orbit in black, and mapped onto the comet's orbital plane (b) depicting a turbulent ion tail with condensation knots and multiple orientation changes. The red diagonal line is the comet's orbit and the red line is the Sun-comet line.

The difference images were chosen for all analysis techniques as they depicted the fine structures more clearly than the calibrated or stacked images. A coadded and dust-subtracted composite image of the nucleus and one of the ion tail, were projected with different observing times onto the comet's orbital plane to create a mosaic stitching image, with the ion tail extending greater than 1°. Different observing times were used to account for the angular and radial motion of the ion tail with respect to the nucleus between exposures. Assuming a solar wind outflow of 400 kms^{-1}, the plasma packets in the ion tail would have covered 3.6 x 10^5 km radially. The timing error for each image is assumed to be half of a minute. For the stacked images, the middle image is taken as the observing time so as to retain the correct astrometric parameters associated with that observing time. For the difference images, the WCS coordinates from each stacked B filter image is used and the relevant r images were distorted till they matched the astrometric coordinates of the stacked B image. The distorted r images were subtracted from the B image to remove the dust contribution.

CR2144

From the Mercator map for CR2144 (Figure 10), there is a reasonable expectation for an observed heliospheric current sheet crossing in mid-December, between 2012 December 12 and 2012 December 13. The observer's projected position onto comet C/2013 R1's orbital plane remained low for the first two weeks of December 2013, only rising to $\sim 20°$ by late December. The orbit plane angle gradually improved, though it remained fairly low, peaking at $\sim 30°$ at the end of the observing period in January 2014. The early set of images, taken in CR 2144, will yield apparent velocities uncharacteristic of the solar wind due to the low orbit plane angle. The orbit plane angle is $< 10°$ for the first half of CR 2144 and between $10°$ and $17°$ for the second half from 2013 December 13 to 2013 December 17. We further expect the comet to be immersed in a fast solar wind region from the 2013 December 26 to 2014 January 09. Thereafter, the comet should experience slower slow wind speeds as it approached the neutral line.

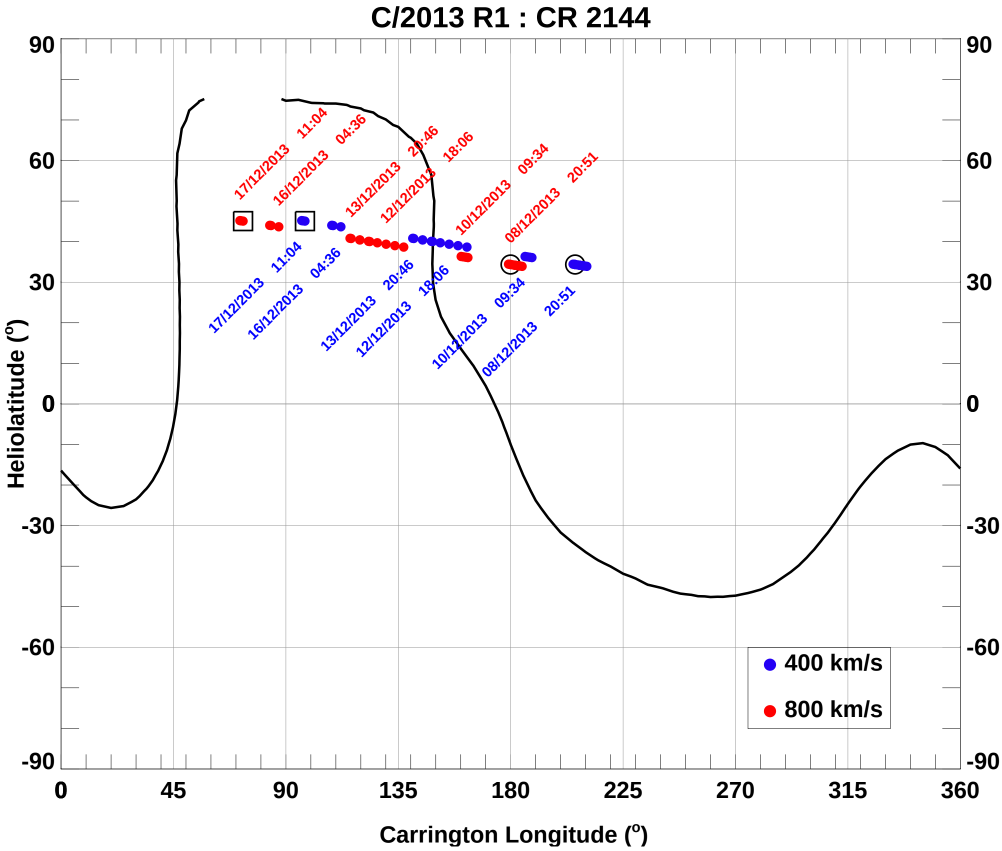

Figure 10. Mercator map for CR 2144 showing expected sources on the solar wind source surface of the solar plasma packets seen to interact with the comet, assuming a fixed velocity for the bimodal solar wind outflow.

The time span from 2013 December 09 to 2013 December 17 were observed at low orbit plane angles, producing v_{sw_r} estimates in the range of 50-200 km s^{-1}. The dust tail and ion tail completely overlapped for most of this period, thus our measurements in Figure 11 are ineffective indicators of the v_{sw_r}. Estimates derived from turbulent ion tail images are highlighted in purple with two DEs identified in the images.

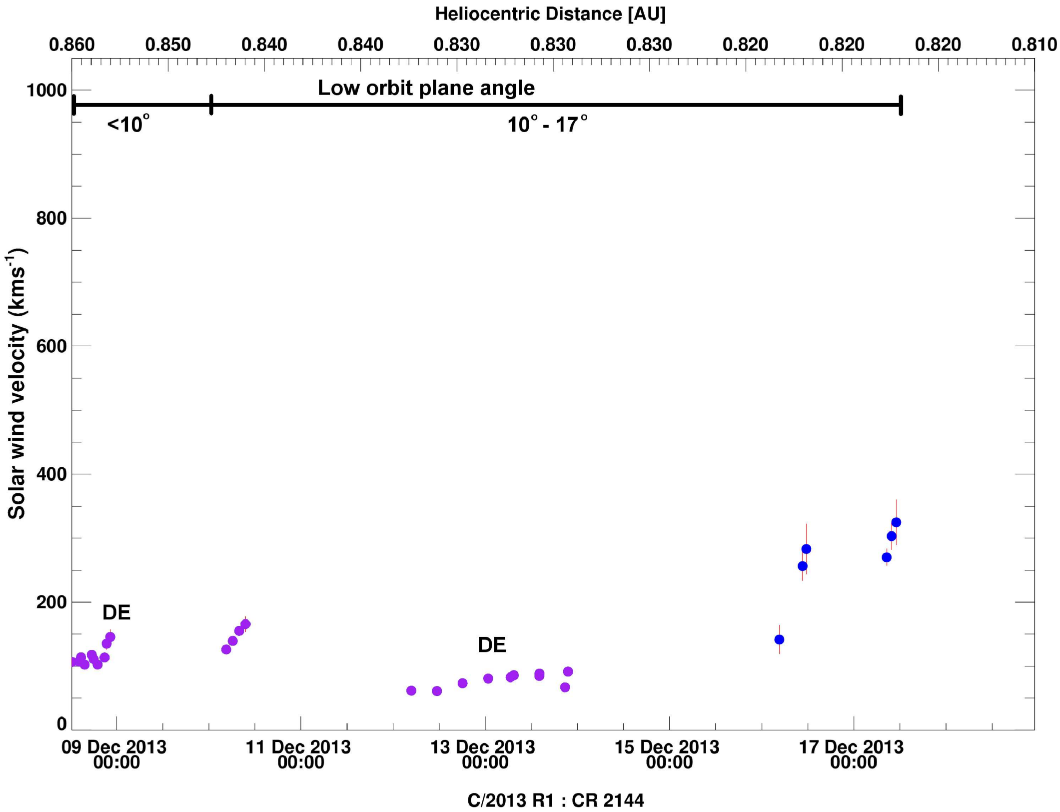

Figure 11. Solar wind velocities from amateur observations of C/2013 R1 during CR 2144.

Figure 12 is one of the best examples of the highly dynamic variations of C/2013 R1's ion tail, with multiple kinks and a disconnection event. The ion tail's orientation varied numerous times and curved back towards the radial vector generally indicating an acceleration of the lagging end of the ion tail. The orbit plane angle remained just below 10° during this time, thus obfuscating the determination of a realistic radial velocity. The structures visible before the near-90° bend in the ion tail direction at ∼5.5 x 10^6 km, seemed to be entrained almost radially when compared with an image by the same observer half an hour later. Simulations generated by the ENLIL 3-D time-dependent heliospheric model (e.g. (Jian et al., 2015) and references therein) predicted low solar wind velocities ∼250 kms^{-1} at the comet with a small latitudinal component (Figure 13). The non-radial component included a reversal of the velocity vector acting upon the comet, thus explaining the arced tail in Figure 12.

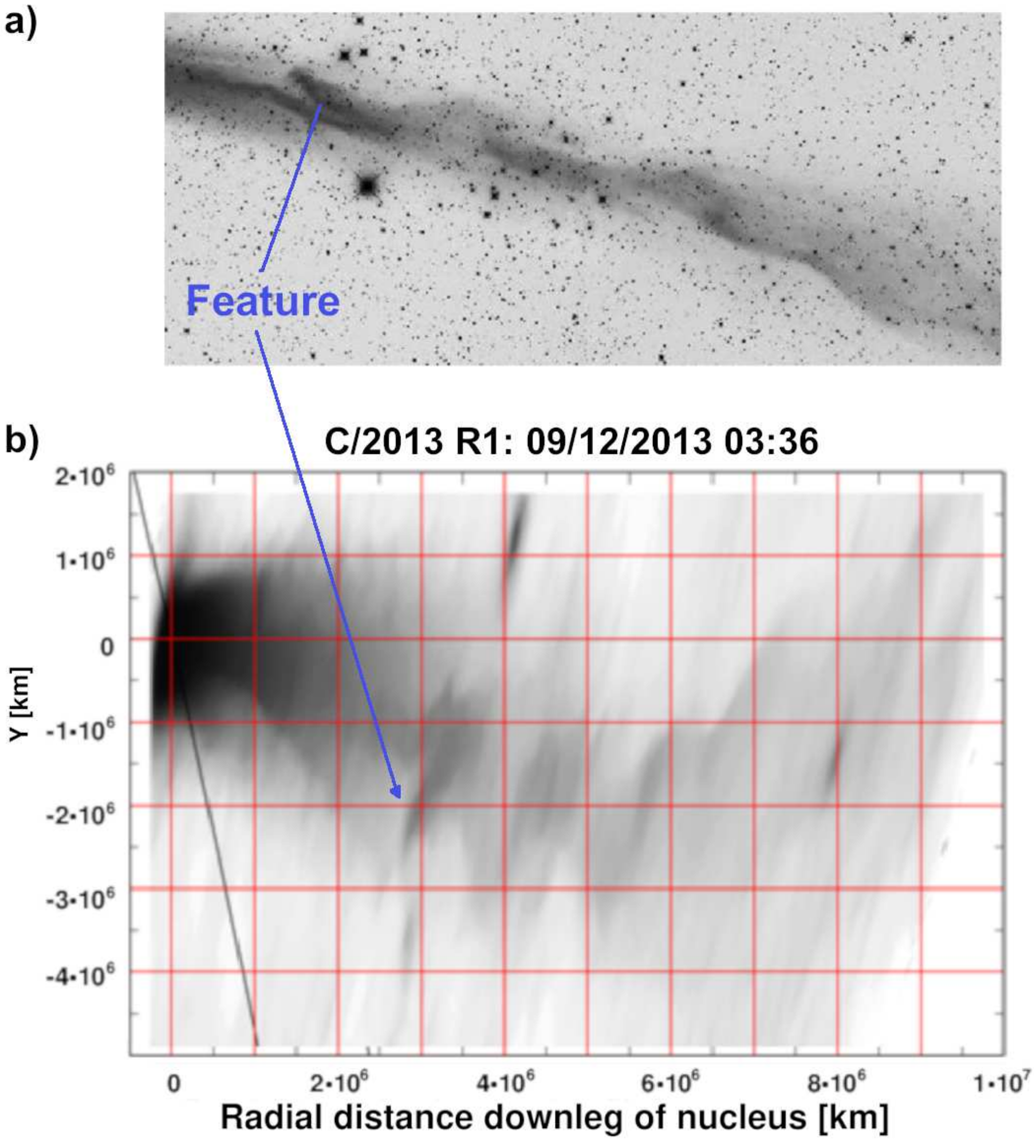

Figure 12. C/2013 R1 captured by Mrozek and Skorupa on 2013 December 09 03:36 UT, showing a tail disconnection (labelled "Feature") and turbulent ion tail. The image has been mapped onto the comets orbital plane in a cometocentric reference frame. Sunward direction is to the left.

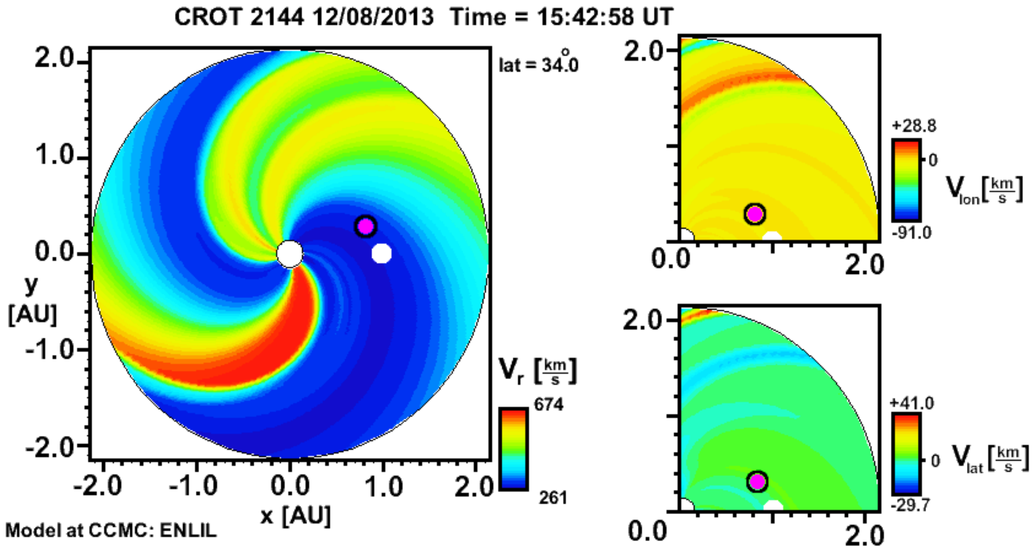

Figure 13. ENLIL MHD simulation for 08/12/2013 at 15:42 UT (CR 2144) at a heliospheric latitude of 34°. The comet was predicted to encounter slow solar wind radial velocities and a non-radial component in the solar wind. The Earth and the comet are shown as the white and magenta dots respectively. The radial solar wind velocity component is shown on the left, longitudinal to the top right and latitudinal to the bottom right.

No velocities were extracted during the expected HCS crossing, as the tail at that time was oriented to actually lead the comet's motion, for which no meaningful radial solar wind speed could be derived. This unusual orientation was presumably due to a significant non-radial component to the local solar wind. The first image, taken by Rhemann on 2013 December 12 (Figure 14a), showed wave-like ripples down the tail and an asymmetrical collection of tail rays. A subsequent image by Rhemann a day later (Figure 14b) showed an equally dynamic tail, with a large condensation knot in the middle with a sharp angular change. This tail behaviour is reminiscent of DEs observed in other comets. The tail was leading the comet motion in both images. ENLIL predicted the comet would encounter opposite HMF polarities ahead of a CIR between 2013 December 14 06:00 UT and December 16 00:00 UT.

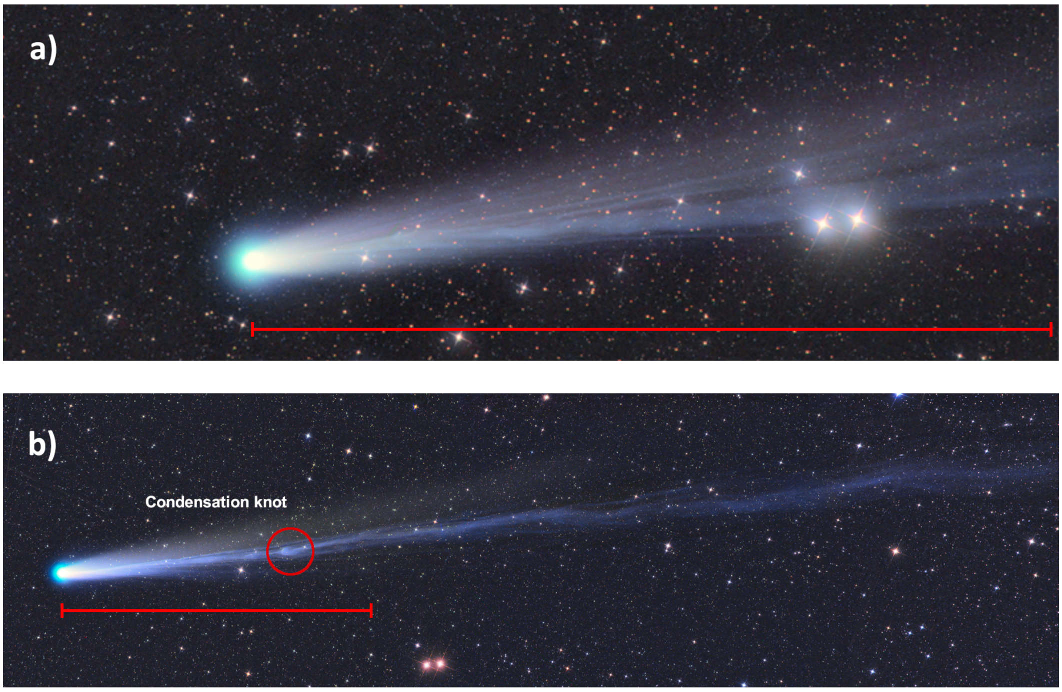

Figure 14. a) Image by G. Rhemann on December 12 04:14 UT with a sharp angular change near the nucleus and asymmetrical tail rays. The two images are of different scale. b) A condensation knot is located close to the nucleus, at approximately one-fifth the ion tail length, with a sinuous ion tail. This observation was by G. Rhemann, on December 13 03:41 UT. The image was edited to highlight the faint structures in the ion tail.

Images taken by Jäger and Rhemann on 2013 December 14 exhibited a very extensive ion tail with a large aberration angle, extending into a wide, faintly connected set of ion cloud packets. The plasma packets, constituting the ion tail are expected to have departed from the approximate location of the comet's ionised coma around 2013 December 12 at $\sim$ 04:00 UT. There is a large kink evident at the point where the ion tail width dramatically increases, suggesting a large HMF orientation change had occurred upstream of the comet. We are likely viewing the ion tail edge-on in the thin section prior to rotation of the ion tail. Large non-radial components are predicted at the time of observation, though this cannot explain the existing ion tail configuration, considering that a low predicted v_{sw_r} of $\sim$250 kms^{-1} would be insufficient to propagate throughout a 1.2×10^7 km tail in time.

ENLIL simulations suggested the comet would encounter the leading edge of a CIR on 2013 December 16. The trend is present in our measurements, though velocities on December 16 and 17 are underestimated by $\sim$ 200 kms^{-1} with respect to ENLIL. The discrepancy throughout this CR is most likely the result of projection effects and the ion tail curving away from the radial direction. This larger perceived aberration would produce much lower apparent solar wind velocities with this technique.

A collection of ICMEs, travelling in the general direction of the comet, and their SATs (Shock Arrival Times) for the periods mentioned previously are shown in Figure 15 and Table 1.The comet's mean position angle was 343° and the position angle of the solar rotation axis was 13°.

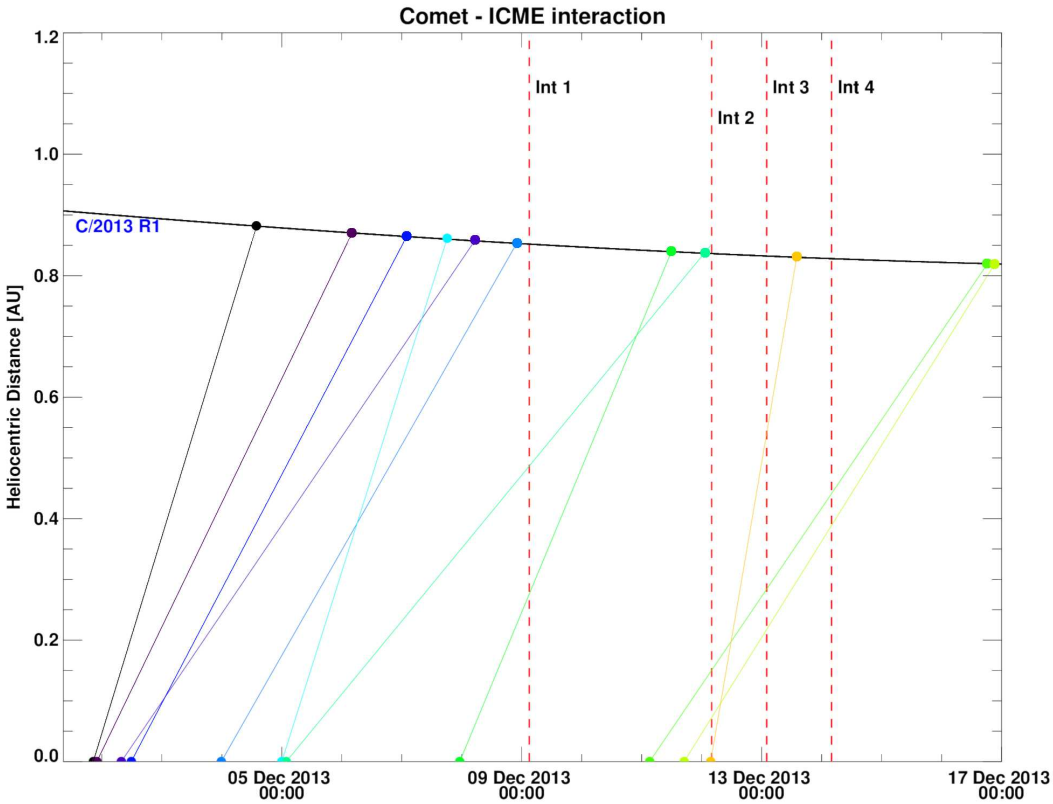

Figure 15. ICME candidates and their potential interaction with C/2013 R1 and their SATs at the comet. The speed of each ICME is based on its plane-of-sky velocity in coronagraph images. A constant velocity is assumed for each ICME propagation. These interactions may have triggered the unexplained disturbances observed in the comet's ion tail. Interactions (labelled as Int 1 to 4) marked above are the approximate times at which the images were taken and not the beginning of the interaction of the ion tail with disturbed solar wind medium. Each coloured line corresponds to a different ICME.

Table 1. The date and time of identified possible ICME interactions at comet are given below using the linear speed of observed ICMEs and the central position angle (CPA), its direction of travel, and the angular width, the approximate expected region of interaction. The speed, direction and angular width is expected to vary as the ICME interacts with its surrounding solar wind medium. We identify the possible interactions for each ICME in the last column.

Date	Time	Linear speed (kms^{-1})	CPA (°)	Angular width (°)	Interaction
2013-12-02	07:48	252	352	56	1
2013-12-02	11:48	326	353	83	1
2013-12-03	23:48	300	331	16	1
2013-12-05	00:00	541	293	91	1
2013-12-05	01:48	208	315	82	2 or 3
2013-12-07	23:12	412	295	116	2 or 3
2013-12-12	03:36	1002	214	276	4

CR2145

v_{sw_r} derived from both the amateur and INT observations are shown in Figure 16. Estimates from turbulent ion tail images are represented as purple dots for amateur images and orange for INT. The range of velocities derived from amateur images is nearly equivalent to the INT images for the period where they both overlap. This fortuitous overlap of observations demonstrates how far consumer technology has come and its benefits to interplanetary heliospheric research.

The data in Figures 16 and 17 suggest that the comet initially encountered slowly decreasing solar wind velocities. This is supported by ENLIL up to 2013 December 25, though predicted velocities at the comet are ∼100 kms^{-1} lower. From ENLIL, the comet was expected to encounter flows of opposite magnetic polarity on December 24 and a CIR with large non-radial flow components on December 25. A high contrast enhanced image on December 24 confirmed a HCS crossing within this time frame.

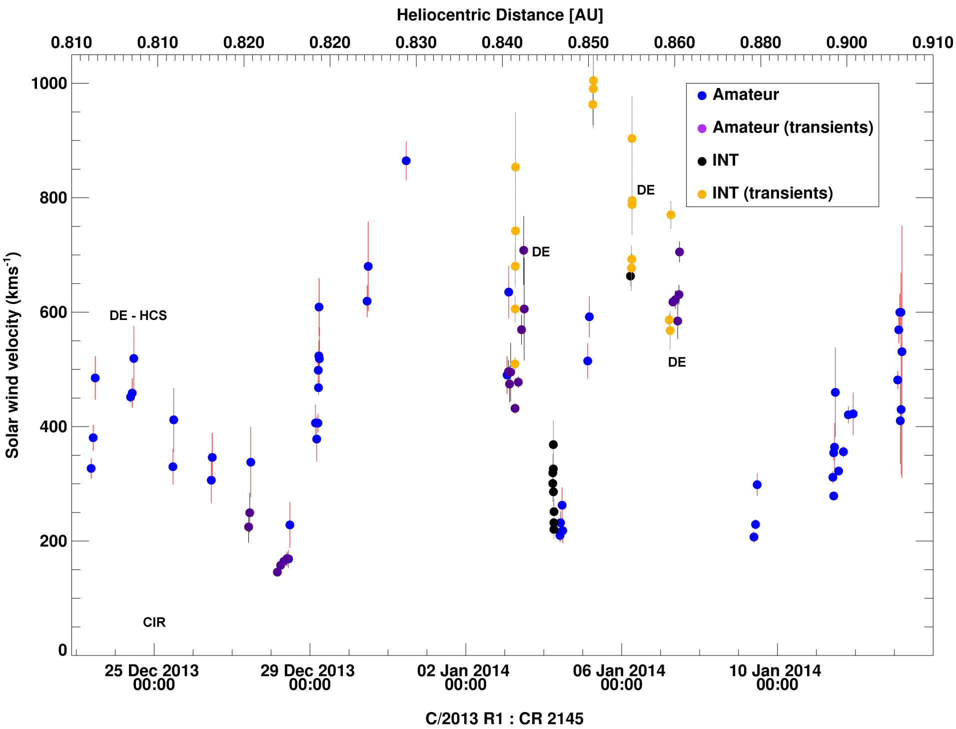

Figure 16. Radial solar wind velocities for CR 2145 derived from amateur (blue) and INT (black) observations. Transient physical structures in the ion tail such as kinks, density enhancements or DEs are marked in purple and orange for amateur and INT observations respectively.

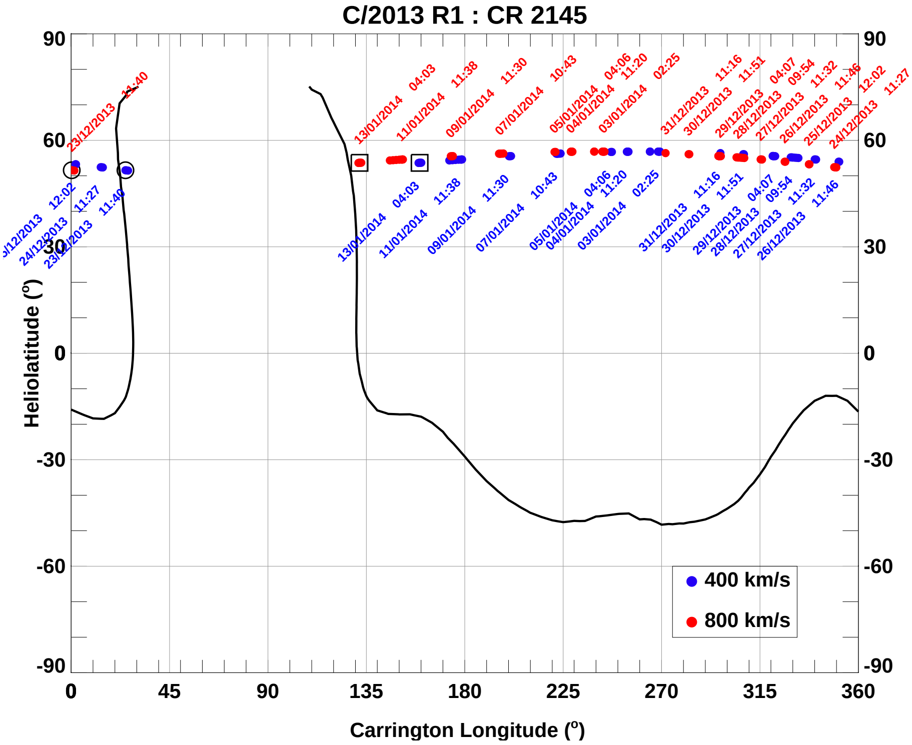

Figure 17. Mercator map for CR 2145. Only sources interacting with the comet in the amateur images have been mapped back to the solar wind source surface. Sources for the INT observations will fall between 2014 January 02 to 2014 January 07.

Direct observational evidence of kinks and a DE contradicted the smooth, fast solar wind outflow predicted at the comet between 2013 December 26 and 28. The comet must have either encountered a slow moving disturbed solar wind, conveniently explaining the decreasing v_{sw_r}, or the high latitudinal MHD solution is incorrect for this run. The sharp increase in velocity on December 29 likely marked the end of the disturbed solar wind outflow with velocities at the end matching expected fast solar wind velocities. The ENLIL fast solar wind region did not show any velocity gradients.

Observations by Rhemann and Jäger on 2014 January 03 caught the onset of an ICME-related turbulent event, with what seemed like small-scale ion tail variations. These propagated and produced a disconnection event observed 8 hours later in an image by D. Peach. The long, sinuous, disconnected tail was measured travelling radially at ~450 kms^{-1}. This was coincident with the INT run where we observed a much closer region of the ion tail. The discrepancy between concurrent results on 2014 January 03 is due to solar wind measurements extracted from the disconnected ion tail over 1×10^7 km versus measurements taken from a newly formed ion tail over 1×10^6 km. The comet experienced a decrease in v_{sw_r} corresponding to a rarefaction region lagging a CIR in the ENLIL model. The velocity samples from both INT and the amateur images are lower than predicted values by ~200 kms^{-1} again. The MHD predicted longitudinal velocity component at the comet is ~20-30 kms^{-1}.

Images from 2014 January 06 showed a DE related knot moving at ~40 kms^{-1}, along and across the tail, and accelerating to ~150 kms^{-1}, as measured from knot movement between images. The condensation knot had a v_{sw_r} of ~700 kms^{-1}. There are no CIRs or DEs expected that match our observations, thus this event was likely ICME related. Turbulence in the ion tail persisted until January 07. INT images showed varying tail orientations and a large trackable kink evolving into a DE 0.25 days later (Figure 18). The comet was not expected to have encountered a polarity reversal in the HMF.

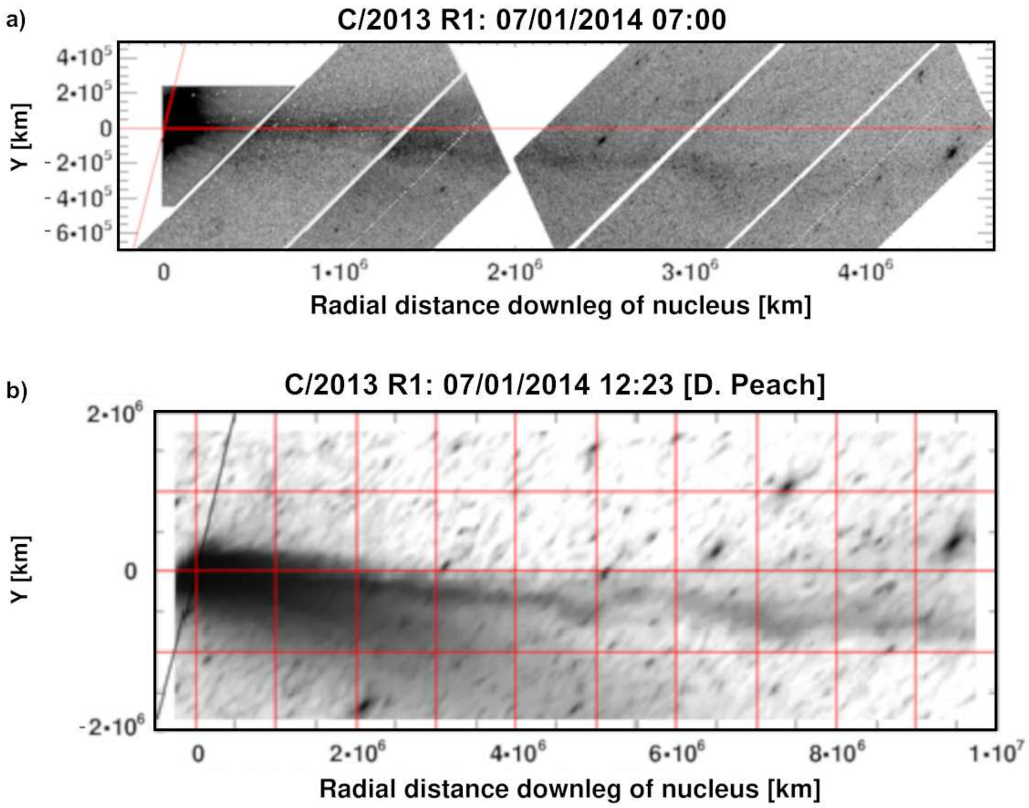

Figure 18. a) Mosaic of stacked, difference image with 5 x Harris B (1 x 10s and 4 x 90s exposures) and 4 x Sloan r images (90s), showing DE at $\sim 1.3\times10^6$ km and kink at $\sim 3\times10^6$ km. b) Amateur image captured by Peach showing the same DE and kink 5.5 hours later, at $\sim 4.7\times10^6$ km and $\sim 7.2\times10^6$ km respectively.

The ENLIL model shows good agreement for SW velocities on 2014 January 09. For January 10, SW velocities ranged between 250 and 450 kms^{-1} and were within the predicted 250 kms^{-1}. There's a slight turbulence and a kink in the ion tail accounting for the range in the velocities reported. There is a small non-radial component to the solar wind on the 2014 January 13 but this does not account for the large discrepancy in the radial velocity of 150-200 kms^{-1} between the observed and the predicted lower values.

A list of potential ICME interaction candidates and their expected arrival times at the comet's location is given in Figure 19 and Table 2. Assuming that the fast ICMEs will slow down upon interaction with the solar wind and conversely for slow ICMEs, the unexplained ionic turbulences described for CR 2145 could be explained by interactions with ICMEs.

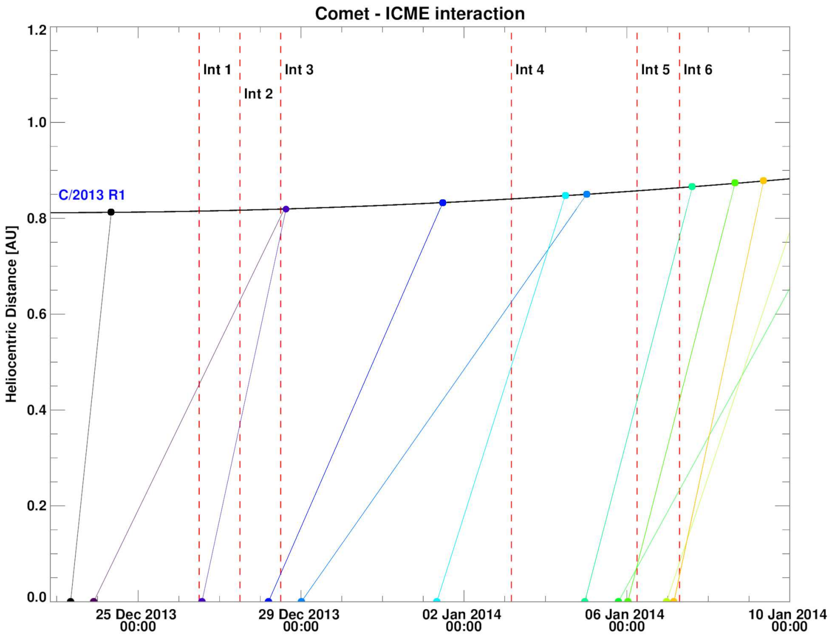

Figure 19. ICME candidates and their potential SATs at comet C/2013 R1. Interactions (labelled as Int 1 to 6) marked above are the approximate times at which the images were taken and not the beginning of the interaction of the ion tail with disturbed solar wind medium. See figure 15 for more details.

Table 2. The date and time of identified possible ICME interactions at comet are given below. See Table 1 for more details.

Date	Time	Linear speed (kms^{-1})	CPA (°)	Angular width (°)	Interaction
2013-12-23	08:12	1409	308	94	1, 2, 3 (maybe)
2013-12-23	21:48	303	312	55	2 and 3 if sped up by fast SW
2013-12-28	04:48	337	355	57	4
2013-12-29	00:12	210	305	85	5 , 6
2014-01-01	08:00	465	291	185	5 , 6

4.1.1 Alternative methods of measuring solar wind velocities

Low orbit plane angle - non radial flow

Several observations during CR 2145 were obtained at low orbit plane angles (Ramanjooloo & Jones, 2021c), allowing estimates of the non-radial velocity components (Figure 20). The ion tail overlapped the extended Sun-comet radial vector. Non-radial velocities of $\sim$45 kms^{-1} were derived from four images with noticeable deviation from the comet's orbital plane.

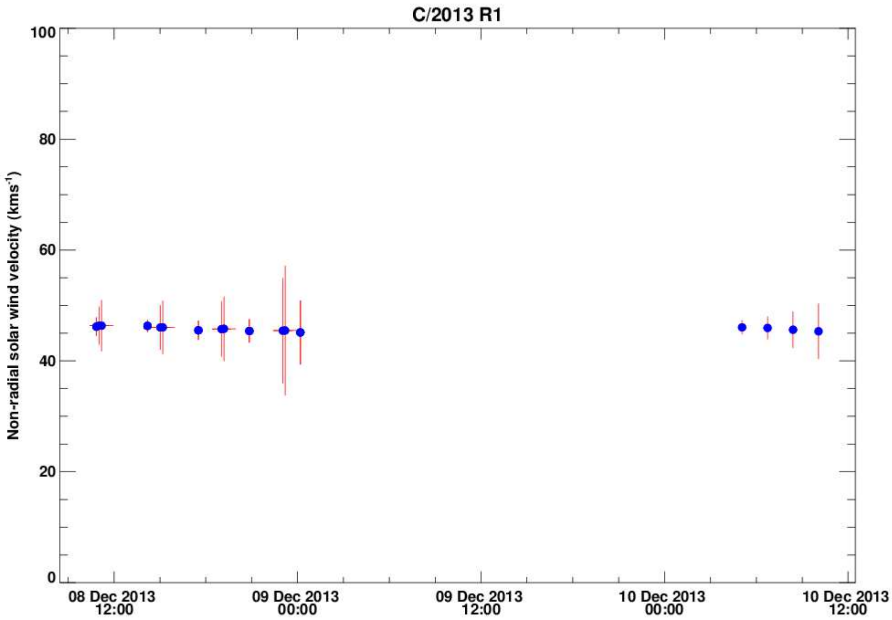

703 **Figure 20.** Non-radial velocity components of C/2013 R1's ion tail. These scenarios arise
704 when the observer's latitudinal angular separation from the comet is small.

705 **Vector Maps**

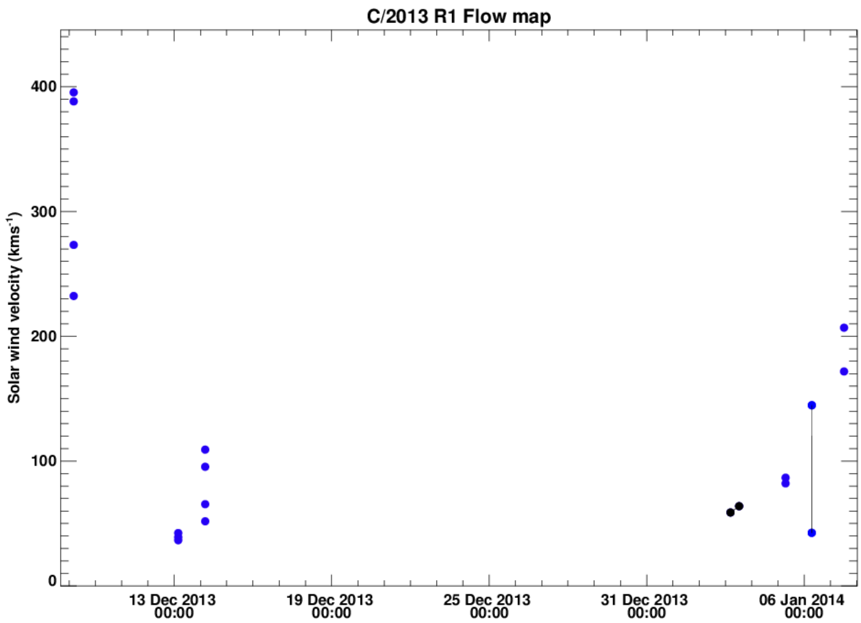

706 **Figure 21.** Velocities of two identified features taken from a sequence of images for comet
707 C/2013 R1. Uncertainties were not included as uncertainties for the first feature was $\pm v_{sw_r}$.

Non-radial velocity measurements [Figure 21] were obtained from sequences of images. The velocity profile was observed to increase downtail of the optocenter as expected of an accelerating ion tail to the local radial solar wind velocity. The first four measurements correspond to two samples from the tracking of a DE and two samples for a large kink in the ion tail. A pair of very slow-moving kinks was tracked, far from the nucleus on 2013 December 14. Measurements were likely impacted by human error due to the large features. A kink was observed to evolve into a slow-moving disconnected tail, with near zero acceleration on 2014 January 06. Bulk radial velocities ranged from 500 to 650 kms^{-1}. INT observations allowed tracking of a DE knot at short cometocentric distances $\sim 5\times10^5$ km. The knot accelerated from 40 kms^{-1} to 140 kms^{-1} within minutes. The initial velocities are in the same range as reported by Yagi et al. (2015) - 20 and 25 kms^{-1} along the tail and 3.8 and 2.2 kms^{-1} across the tail.

Tracking an expanding amorphous cloud proved to be challenging in the absence of information on its expansion rate, direction and center. Tracking an approximate knot center was found to be heuristically better than tracking the features edges. Measurements are therefore subjective and slight variations in the feature center can translate to significant changes in the velocity. The feature was observed on 2014 January 06 at $\sim 1\times10^6$ km from the nucleus. We measured a mostly linear acceleration of the plasma packet down the tail. The trending radial velocity along the tail was $\sim$60 kms^{-1} $\pm$ 60 kms^{-1} and non-radial velocity of 10 kms^{-1} $\pm$ 54 kms^{-1} across the tail.

4.1.2 Tail rays

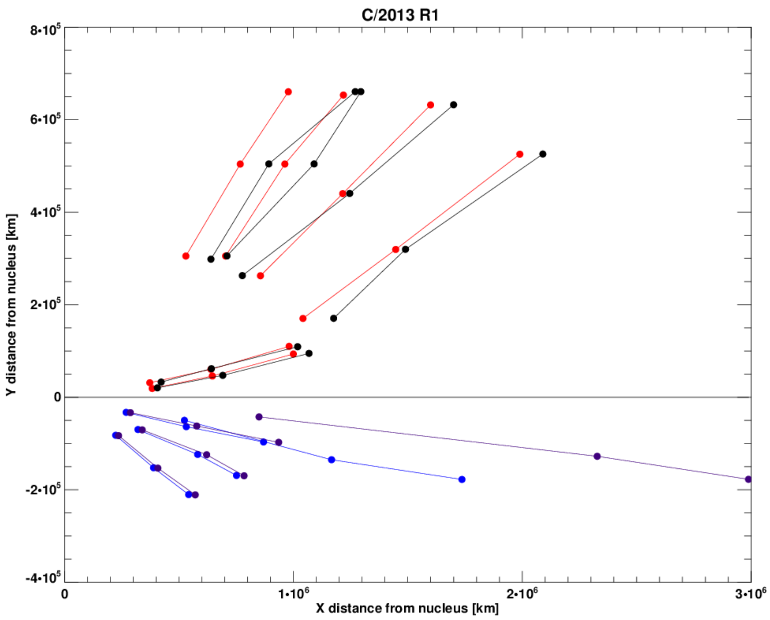

Figure 22. Measured samples of folding tail rays for comet C/2013 R1 are taken in sets of 3. Measurements are taken from two consecutive images. The red and black dots are positions taken folding ion tail rays above the Sun-comet line in images 1 and 2 respectively. Blue and purple dots are measured positions below the Sun-comet line from images 1 and 2 respectively. Each set of measurements are connected by a line to represent that they are from the same folding ray. We can thus track the evolution of the tail ray between images.

We define top and bottom tail rays as tail rays located above and below the Sun-comet line respectively (Figure 22). The comet exhibited multiple top tail rays close to each other making it difficult to delineate the tail rays positions along the extended radial vector. The bottom tail ray was extensive ($\sim 3\times 10^6$ km) and folded quickly about the main tail axis, producing velocities close to the slow v_{sw}. The top tail rays appeared curved. Aside from a few outliers, the v_{sw} increased with both time (Figure 23a) and cometocentric distance (Figure 23b) or remained near-constant. These outliers, mostly in the top tail rays, were measured from curved tail rays indicating a disturbed solar wind flow interfering with the expected evolution of tail rays. The viewing geometry likely compounded this effect. From 2014 January 03 to 07, the folding ion tail rays were evident in the close-up INT images. However, the brightness stretching tool were inefficient at separating the tail rays for reliable measurement. The results shown here should be treated with caution.

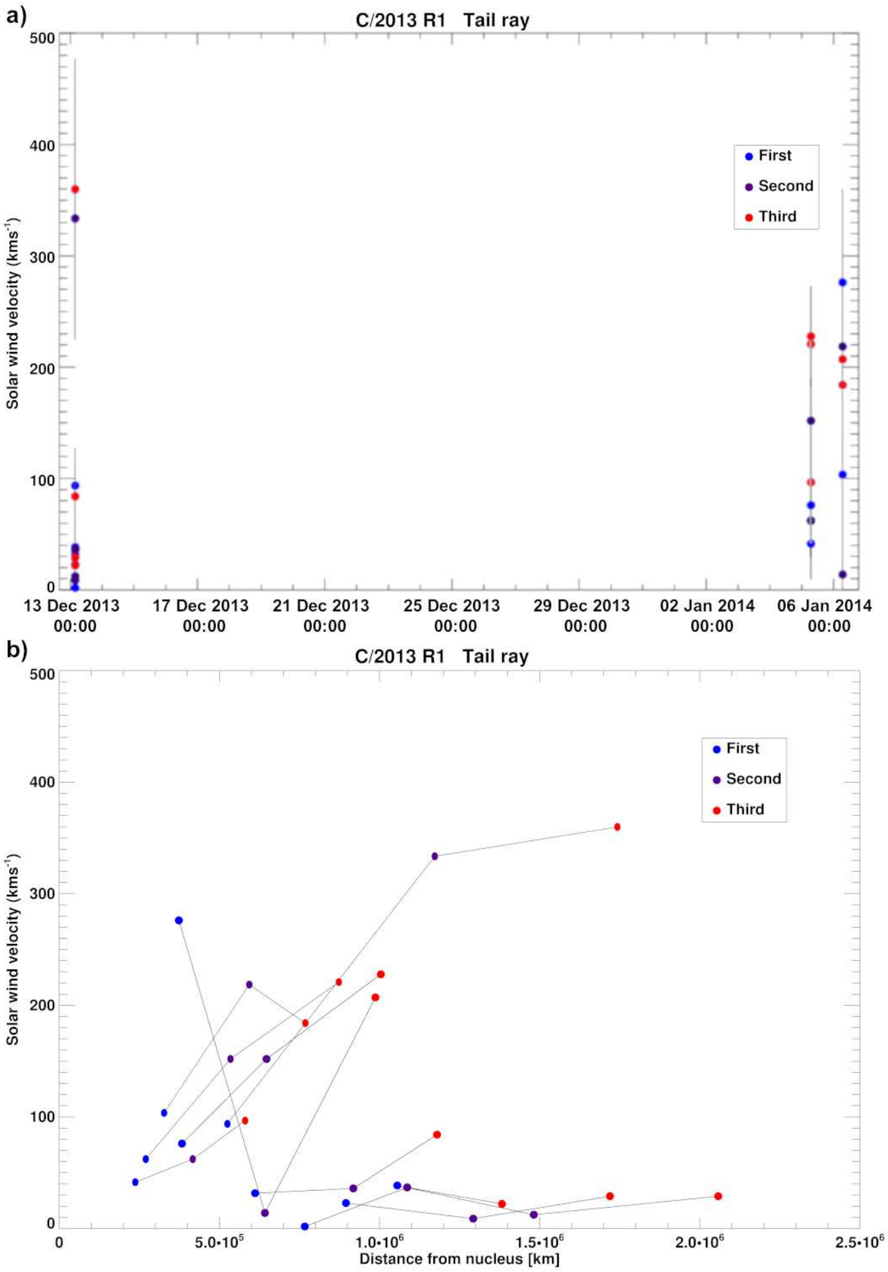

Figure 23. v_{sw} with respect to time (a) and radial distance (b) from nucleus. The first (blue), second (purple) and third dot (red) represent the three measurements taken in each set. First is closest to the nucleus and third is furthest along the folding ion ray. As expected, we mostly see an increase in velocity away from the comet.

4.1.3 Conclusion

v_{sw_r} measurements near the nucleus were consistently higher than velocities further down the tail contrary to theoretical expectations. We would expect the solar wind to become mass-loaded through the cometary pick-up ion process as it approaches the comet's nucleus. The mass-loaded solar wind would then accelerate down the tail until it reaches the surrounding solar wind velocity. A distinct curvature to the ion tail was present in most of the mapped images, with the degree of curvature lessening with decreasing cometocentric distance. This unique morphology when mapped is the primary reason for the range of measured velocities. The INT observations were all taken within 1.5×10^6 km of the nucleus, with moving features identified and tracked as close as 5×10^5 km. During our analysis of the amateur images, the dust tail and ion tail overlapped due to the observing geometry although this was mostly not a hindrance during data extraction. All the velocities derived for this comet were taken when the orbit plane angle was $\sim 20°$. Contrary to previous comets, the ENLIL MHD visualisations offered little insight into the chaotic episodic flows observed at the comet. These sudden deviations from the fast v_{sw} can only be explained by ICME interactions since no HCS crossing or slow winds were expected. We report excellent agreement between the solar wind velocities derived from amateur images and a professional grade observatory for both the regular solar wind flow and transient features in the ion tail. This suggests that amateur observations afflicted by inclement weather and subjected to likely worse seeing conditions are as reliable.

4.2 C/2011 L4 (Pan-STARRS)

Discovered on 2011 June 6 (Wainscoat et al., 2011), the first apparition of C/2011 L4 (Combi et al., 2014) was well observed both from Earth and STEREO B, with a brief observation by STEREO A. C/2011 L4's most striking feature was an extensive striated dust tail. The object reached its 0.30 AU perihelion on 2013 March 10. All dates in this section refer to the year 2013.

4.2.1 Ground based observations

Only 3 samples could be extracted from 1 image out of 41 fully processed images post-perihelion, as most images did not have an observable ion tail. The ion tail, when observed, was extensive, straight and very close to the radial vector and lacked any features usually associated with a turbulent solar wind flow. Velocities, measured along the tail, ranged from 1100 to 1400 kms^{-1}. No distinct cause of the extreme high velocities could be identified. Amateur images of C/2011 L4 were seldom exposed for long enough to image the ion tail. The comet's extensive and bright dust tail overlapped with the ion tails orientation, further complicating the latter's study. The other images in our catalogue were unusable as the Earth traversed the comet's orbit in late May 2013; our technique failed due to the low orbit plane angle.

4.2.2 STEREO B

A total of 742 v_{sw_r} estimates were extracted from 190 difference images (Ramanjooloo & Jones, 2021a). 7 images were rejected due to the ion tail's proximity to the dust tail or image defects, which would have rendered the analysis unreliable. C/2011 L4 showed no evidence of folding ion tail rays. There were a number of turbulent periods. This comet was an ideal target for the velocity vector map, as the ion tail was very dynamic, leading a wide and very bright, well-structured dust tail. The ion tail lagged behind what we interpret to be the comet's neutral atom tail (Fulle et al., 2007). We note that Raouafi, Lisse, Stenborg, Jones, and Schmidt (2015) in fact interpret the northernmost tail to be the ion tail, with the second, highly structured and dynamic tail studied by that team being dust. The lack of any changes in the northernmost tail are strong indications that it was instead a neutral atom tail. Difference images revealed an aberrant, sinuous ion tail that extended over a large extent of the observations with multiple plasma blobs and DEs as the comet left the STEREO HI-1B FOV. The results oscillated about conventional slow solar wind velocities. The variations seen in the later measurements corresponded to large orientation changes and increase in turbulent dynamicity in the ion tail.

On March 13, the comet appeared to have two ion tails, one stemming from the expected location, the other jutting out from one of the top dust striae.

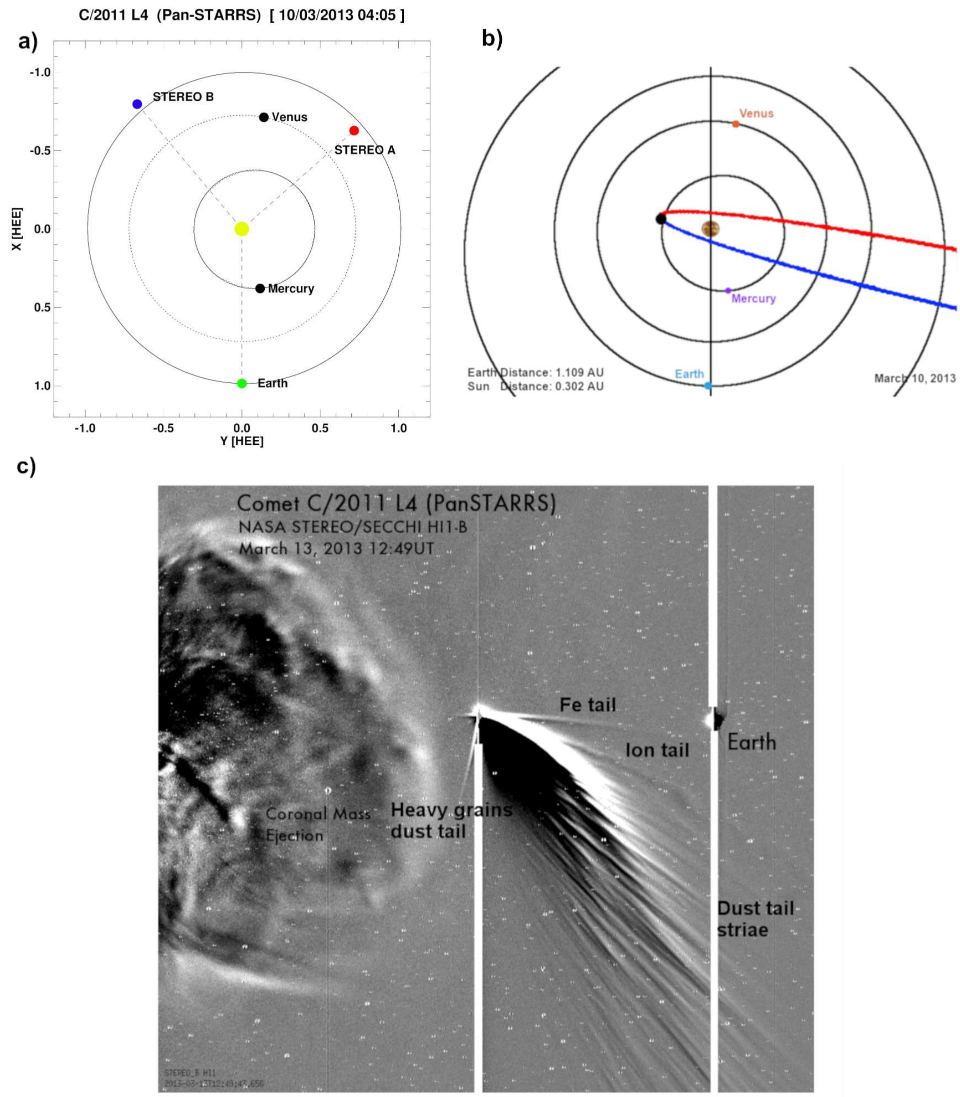

Figure 24. (a) Orbit geometry of the multiple vantage points in Helicoentric Earth Ecliptic (HEE) coordinates from which C/2011 L4 (Pan-STARRS) was observed at the comet's perihelion. (b) Image adapted from the JPL small-body database showing the comet's orbit on the day of its perihelion (March 10, 2013). (c) Difference image of C/2011 L4 from STEREO B on March 13, 2013, 3 days after perihelion. We label the uniform iron (Fe) tail, the variable ion tail and the striated dust tail which made this a unique comet.

Our period of analysis started shortly after perihelion, and extended from March 10.673 UT to 16.478 UT, when the comet was moving from southward (blue) to northward of the ecliptic plane (red) (Figure 24b). Although this geometry was disadvantageous for ground-based ion tail observations, STEREO B was well positioned on the far side of the Sun from Earth (Figure 24a). An image captured by STEREO B 3 days after perihelion shows a uniform iron (Fe) tail, a striated dust tail with a dynamic and variable ion tail in between (Figure 24c). The orbit plane angle for STEREO B remained stable (figure 25b) and large enough to produce reliable solar wind estimates; that of Earth (25a) clearly shows the poorer observing geometry.

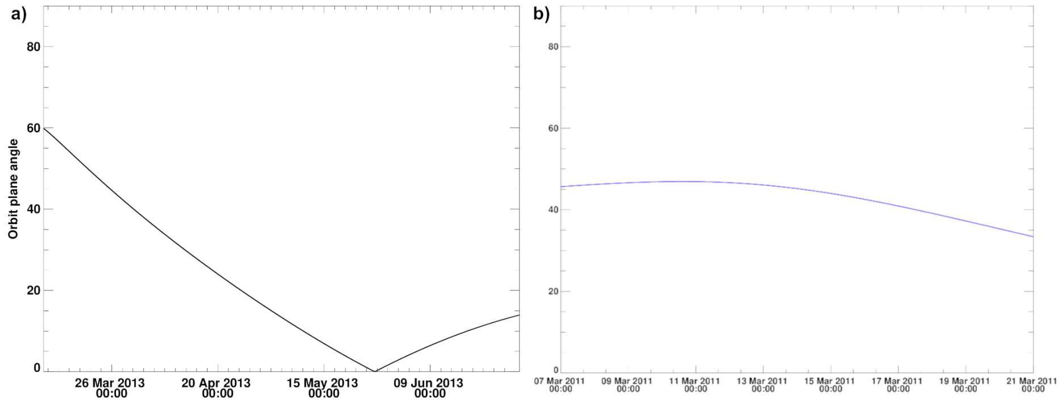

Figure 25. Orbit plane angle of comet C/2011 L4 from (a) Earth and (b) STEREO B.

Assuming a bimodal distribution of v_{sw_r} of 400 and 800 kms^{-1} (Figure 26), we can estimate the approximate origins of the solar wind plasma at its source surface. The predicted sources on the Mercator map corroborate the v_{sw_r} estimates we derive from comet C/2011 L4 as we expected to mostly encounter a turbulent, streamer belt flow of the slow solar wind. According to the Mercator map, the comet encountered the HCS between March 14 and 15. STEREO-B images provided continuous monitoring of the comet crossing the HCS and the resultant DE. The tail likely detached around 2013 March 15 00:00 UT, followed by an outflow of multiple distinct condensation knots over several hours. A large change in the tail orientation change occurred between 12:09 and 16:09 UT. A data gap occurred around 2013 March 15 00:00 UT.

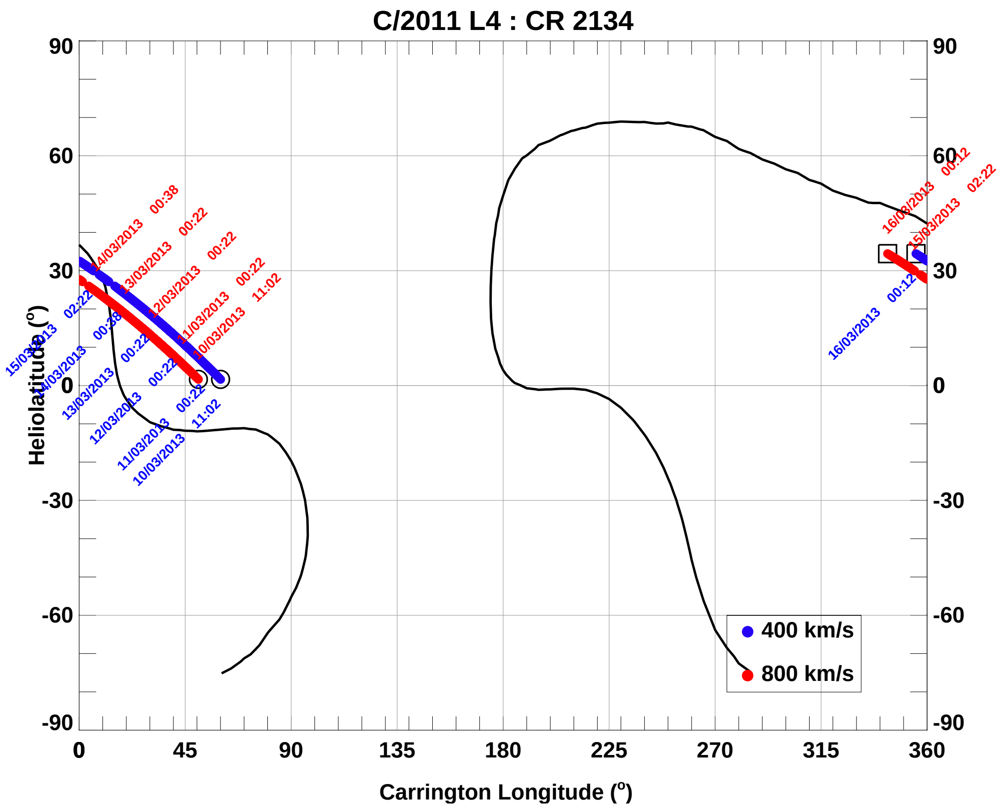

Figure 26. Mercator map for CR 2134. The comet was expected to experience slow v_{sw} as it sampled solar wind from sources closer to the neutral line.

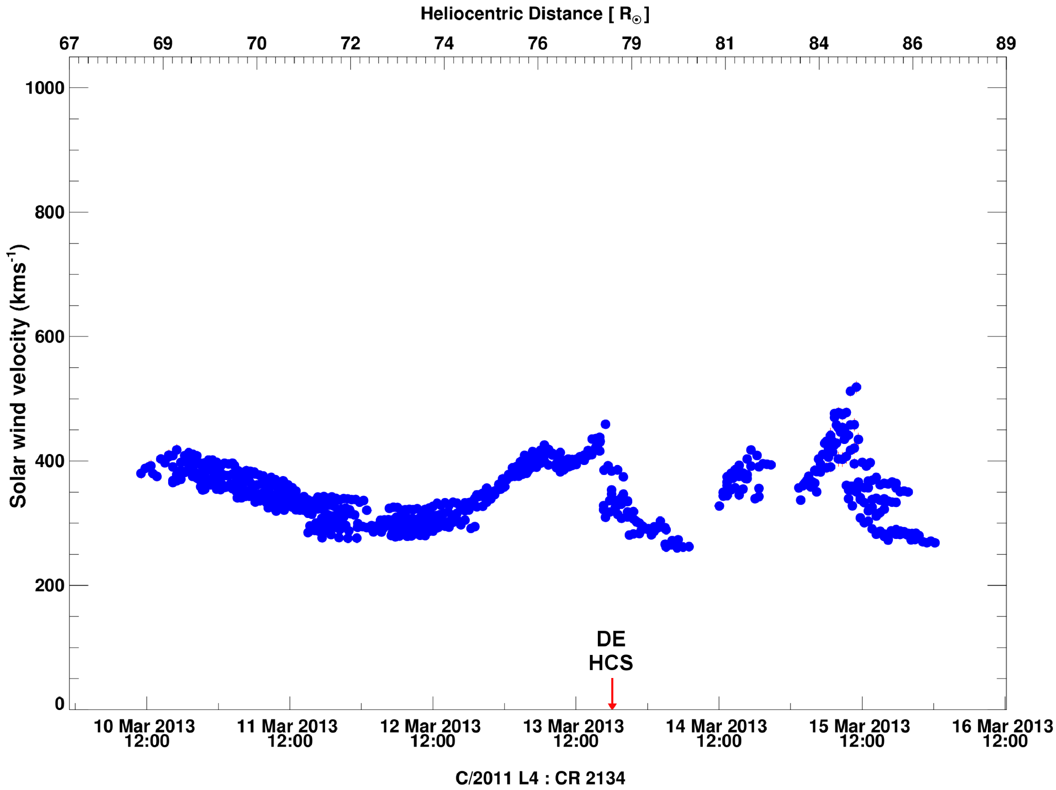

Figure 27. Post-perihelion solar wind velocities for C/2011 L4, based on observations with STEREO HI-1B. Heliocentric range sampled in AU: ∼0.302 AU to ∼0.349 AU. Error bars are given in red however most are smaller than the blue dots.

The comet's outbound trajectory sampled solar wind between heliocentric distance (r_H) ∼68 $R_\odot$ (∼0.316 AU) and ∼87 $R_\odot$ (∼0.405 AU). The velocities match well with the ENLIL predictions. The MHD model predicted a velocity drop from ∼400 to 250 kms^{-1}, a steady slow solar wind of ∼250 kms^{-1} up to March 14, when it would encounter a moderately fast solar wind. This would correspond to a speed hump of 450 – 550 kms^{-1} starting March 14 ∼12:00 UT and lasting for two days. The velocity peak would occur at approximately 2013 March 15 21:00 UT, when we registered a decreasing solar wind flow. The start of the enhanced v_{sw} region matched well with our data, though the ensuing period indicated that the comet would have traversed the fast solar wind region by March 15 18:00 UT. It should be noted that this region was associated with notably large longitudinal and latitudinal non-radial velocity components (∼ 20kms^{-1} for both). The expected velocity peak also agreed well with our results (Figure 27). The deviation from the MHD model occurred during the previously described continuous condensation knots at the predicted HCS crossing. It is far more likely that this turbulent period is associated with an ICME-on-ICME interaction from the last two ICMEs reported in Table 3 and Figure 28. In addition, the ICMEs could simply have decelerated, e.g. Grison et al. (2018), to the ambient slow v_{sw} of ∼250 kms^{-1}. The possible merging of the two ICMEs would have resulted in a complex ICME-solar wind outflow at the comet, which may have compressed the fast solar wind ahead.

Table 3. The date and time of identified possible ICME interactions at comet are given below. See Table 1 for more details. The comet is between position angles 95° to 55°.

Date	Time (UT)	Linear Speed (kms^{-1})	CPA (°)	Angular Width (°)
2013 March 11	13:48	241	93	116
2013 March 12	10:36	1024	74	196
2013 March 12	23:48	481	1	112
2013 March 13	00:24	523	124	127

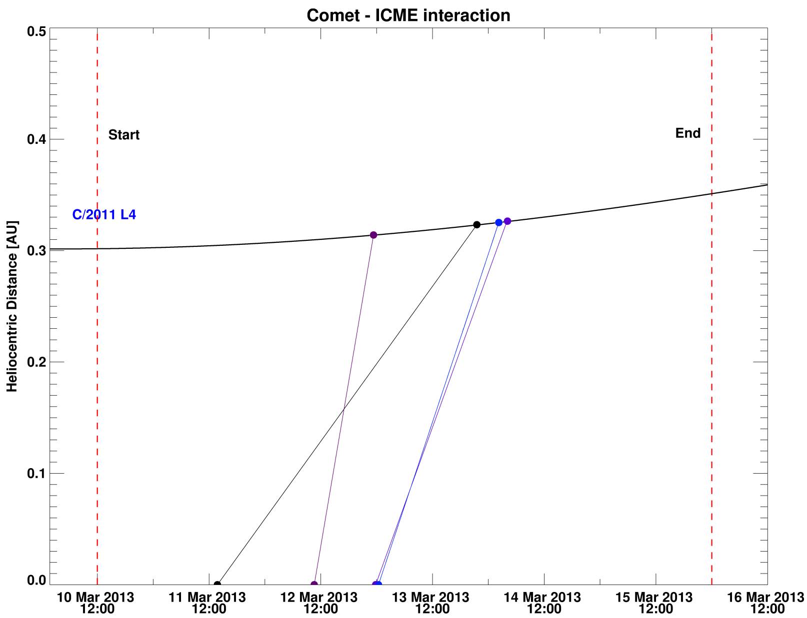

Figure 28. ICME candidates and their potential SATs at comet C/2011 L4. The start and end of the STEREO B observations are marked as red dotted lines. These interactions may have triggered the dynamically variable ion tail structures observed during this period. Each coloured line corresponds to a different ICME. The overlap between the first two ICME paths suggest they may have interacted with each other, slowed down and could have interacted further with ICME 3 and 4.

The density enhancements $\sim 1\times10^7$ km from comet head, observed at March 12 22:09 UT, coincided well with the expected arrival of a fast ICME, observed at the comet at March 12 10:36 UT (Table 3), at the comet. A double dynamically responsive tail with fairly similar initial propagation direction, was observed emerging in close proximity to the extensive dust tail. The two tails appear to cross over at $\sim$1.3-1.4$\times10^7$ km, followed by a DE. The morphology of the bottom tail is that of a dust stria, which may have undergone a clumping of dust grains. It is unclear whether the second density enhancement is dust or plasma. The CORHEL MHD predicted two polarity reversals at the comet on 2013 March 12 $\sim$09:00 UT and 2013 March 13 $\sim$15:40 UT (Figure 29). There are no tail DE identified due to large data gaps and image processing defects during the first period. The second polarity reversal is expected around March 13 18:00 UT, matching well with the observed formation of a DE at 18:49 UT in the STEREO A images (not included in this analysis due to the poor observing geometry). The disconnected tail also coincided with the edge of the merged ICME around the same time. The second highest maxima in the velocity distribution on 2013 March 13 ∼18:00 UT are velocities from the disconnected tail.

It remains unclear as to why the ion tail underwent a large orientation change at March 15 13:29 UT, at a cometocentric distance of $\sim 6\times10^6$ km. This would have been initiated slightly earlier at the comet's head. A very faint solar wind plasma cloud can be seen in the larger STEREO HI-1B FOV possibly arriving at the comet at 06:09 UT, whilst the comet was already displaying turbulent ion tail flow. It is evident that the comet traversed a disturbed medium, which likely corresponds to the merged ICMEs. The link between the two is tenuous, though it is the only obvious solar wind phenomenon that could account for the atypical ion tail behaviour.

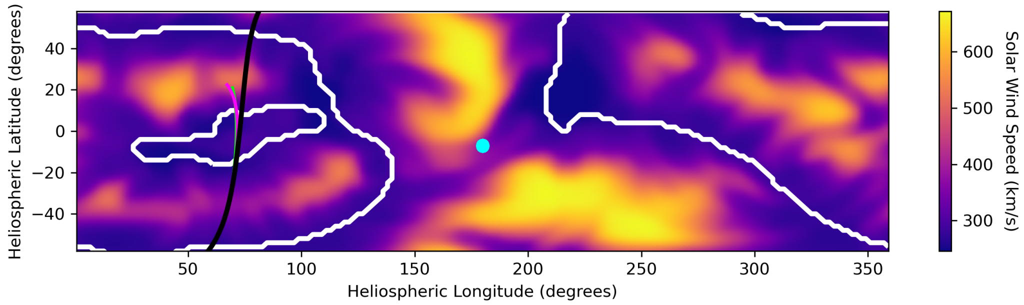

Figure 29. Polarity map for the CORHEL MHD model for CR2134 predicting two DEs connected to sector boundary crossings. The comet's source track is plotted in black, and the sub-Earth position is shown with a blue dot. Map courtesey of O. Price.

4.2.3 Flow Vector Maps: Non-radial velocity

Prominent features in the disturbed ion tail maintained their radial motion with no spurious off-radial motions. Most features were hence tracked at a cadence of 80 mins. Each feature tracked between consecutive images is represented with the same colour and connected with a line. We then group these features per time period for as long as we could track these short-lived features. These are labelled as sets 1 to 7 (Figure 30a). At certain points, for example on 2013 March 13 00:29 UT to 03:29 UT, the comet appeared to have two ion tails (feature set 2). Both were measured in the vector maps, although only the northernmost tail, the real ion tail, was included in the radial velocity investigation.

It is difficult to make sense of these velocities, though they mostly show solar wind velocities centered about reasonable values of $\sim$300 kms^{-1}. Feature set 3 followed the acceleration of a kink and a potential disconnected ion tail as it accelerated to ambient v_{sw}. The root cause of this disconnection was not identified. Set 4 corresponds to the HCS tail disconnection. The corresponding tail feature slowed down initially, forming a kinked tail. Once disconnected, the tail section rapidly accelerated to 240 kms^{-1}, close to the MHD predicted v_{sw}, followed by a decrease in acceleration. A radial velocity interpretation of this image produced a v_{sw_r} of $\sim$400 kms^{-1}, further reinforcing the view that tracking DEs produces slightly erroneous solar wind velocities. This is because the disconnected tail would appear to momentarily not respond to the radial solar wind flow. Feature set 5 was taken from a particularly complex difference image, which had been linked to a period of ICME-ICME interaction with the ion tail. The differing trend between different sections of the ion tail is further evidence of a complex non-radial flow at the comet. Small velocity variations could be due to human error. This dataset fills in the velocity data gap in Figure 27, though there is a clear mismatch between the two techniques. The last 5 features can be separated into two groups. The first (feature set 6) was measured from the second half of the poorly processed difference images and tracked the formation of a newly formed turbulent ion tail. This new tail segment corresponds to the large orientation change, also linked to an interaction with the ICME-ICME disturbed medium. The final feature, set 7, correlates well with the radial velocity technique, supporting our hypothesis that the comet will have traversed the coronal hole more quickly than predicted by the ENLIL model.

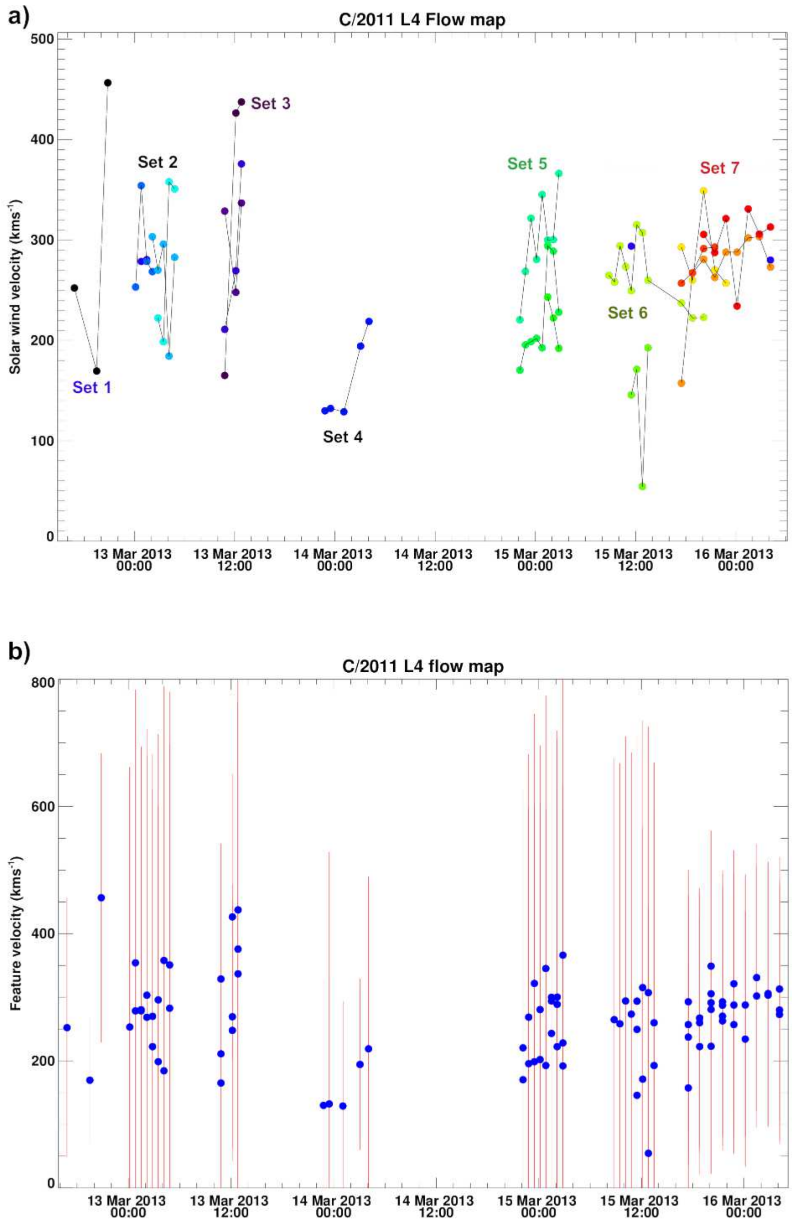

Figure 30. Solar wind velocities derived from consecutive difference images showing the evolution of distinct features in the ion tail. (a) shows each tracked feature linked together to show the velocity variations. (b) shows the large uncertainties for each estimate .

4.2.4 Discussion

Overall, C/2011 L4 proved to be an interesting probe of the turbulent streamer belt region of the solar wind usually seen at low heliolatitudes (Figure 31), as solar cycle 24 approached its maximum.

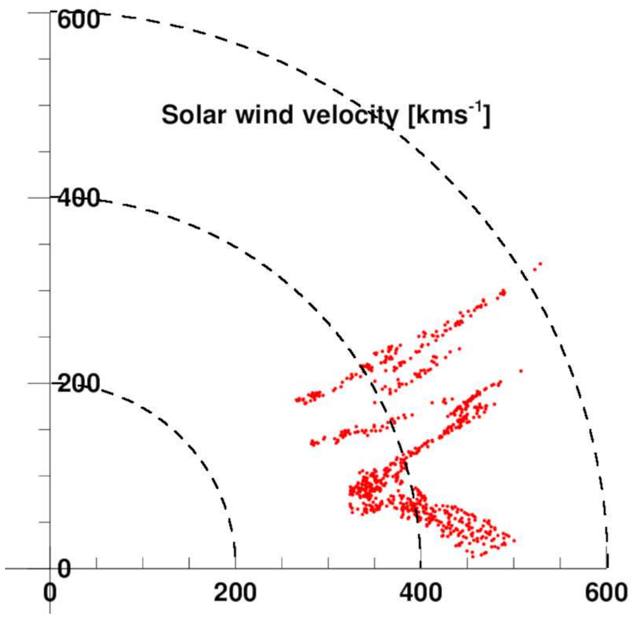

Figure 31. A polar plot of solar wind velocities from C/2011 L4, showing the heliographic latitudes of the measurements (the solar north pole being vertical in this view, and the equator horizontal). The circles represent isovelocity contours for a fixed v_{sw_r} at increments of 200 kms^{-1} from 0° to +90°.

The measured solar wind velocities for comet C/2001 L4 are within expected values for the slow solar wind. They correlated well with the predicted ENLIL MHD-derived velocities. The STEREO B image archive consisted of numerous images taken at a fixed cadence over several days, allowing the near-continuous monitoring of the comet's behaviour near the Sun. The spacecraft data yielded a greater number of data points for the v_{sw_r} than the amateur observations, as the ion tail extended over greater distances than was typical for amateur images. The velocities were tightly correlated with lower velocity uncertainties over longer cometocentric distances. C/2011 L4 was a near-Sun comet that probed regions of the solar wind close to the Sun which had been heretofore difficult to sample.

5 Discussion

5.1 Solar Wind velocity comparison

There are few published large scale studies of the solar wind based on comets' ion tails. J. C. Brandt and Heise (1970) undertook a statistical analysis of comet ion tail orientations, which suggested mean radial velocities of 450 ± 11 kms^{-1} with a tangential component of 8.4 ± 1.3 kms^{-1}. They further proposed a revision of their previously quoted lower bound of the v_{sw_r} from 150 to 225 kms^{-1}, which is in accordance with our estimates and *in situ* values.

The data scatter of v_{sw_r} from spacecraft images was quite well constrained due to the high-quality of consistent observing and data reduction procedures as well as the lack of an atmosphere influencing the image quality. Spacecraft in situ sampling remains the best and most accurate method of providing detailed information on the solar wind. The remote sensing techniques used in our software provide an alternative inexpensive crowd-sourced solution to increase our spatial and temporal sampling of solar wind velocities and transient phenomena in the inner heliosphere.

The close agreement between our results and the ENLIL MHD model demonstrate the potential to devolve the dynamical ion tail aberration into a series of velocities as long as we adhere to a strict set of imaging standards and conformity. To account for v_{sw} discrepancies with the CCMC ENLIL model predictions we attempted to identify a cause of transient disturbances in the solar wind flow. Sizonenko (2007) pointed out similar discrepancies between their solar wind velocities derived from comet observations and those measured by space-based instruments. They linked these to the low accuracy of cometary observations and to differing solar wind conditions experienced by Earth and the comet, although they had no clear cause. It is unclear how much of an effect the observing geometry contributed towards these discrepancies. Sizonenko (2007) reported that there may be an unaccounted force which could have affected their observed velocities.

A more in-depth study assessing the data quality of spaceborne observations against ground-based amateur images would be useful to further validate this technique. This would require a sufficiently large temporal overlap between the two vantage points. This is difficult to achieve as the solar-observing spacecraft will image comets at low solar elongation when they are at their most difficult to observe from Earth.

Tracking the radial evolution of folding tail rays using the mapped images is a theoretically sound concept. Accurately pinpointing the radial locations of the tail rays requires a smaller scale contrast between the tail rays and the image FOV than is available with amateur images. A series of images taken with an hourly cadence, or better, and small FOV is highly recommended for this technique.

5.1.1 Low orbit plane angle

It is notable that there is a systematic overestimation or underestimation of the v_{sw}. This is likely due to the orbit plane angle and the observing geometry. At low angles, the projection mapping breaks down as the pixel vectors are stretched to near-infinity when the orbit plane angle approaches zero.

In the JPL Horizons data, positive values of the orbit plane angle indicate that the observer is above the comet's orbital plane along the positive z-axis in the inertial reference frame. Our orbit plane angle plots only show the absolute value, as it is assumed that the observer's location above or below the comet's orbital plane is irrelevant. In an idealised scenario for a straight ion tail with no complications, the geometry reduces to the three-dimensional position of the observer with respect to the comet and the extended Sun-comet radial vector. Assuming the anti-sunward solar wind flow at the comet is purely radial, the ion tail will be constrained to the plane of the comet's orbit. When the observer is ahead of the comet, with the Sun-comet line between the observer and the ion tail, the projected uncertainty will always be underestimated, regardless of the observer's z-position with respect to the comet's orbital plane. Vice versa, when the observer is lagging the comet's motion such that the ion tail flows between the observer and the Sun-comet vector, the projected ion tail will appear to have a smaller aberration angle. In a realistic situation, factoring in a curving ion tail from radial speed variations and non-radial plasma flows, the orbit plane angle becomes an important criterion in the distorted projection.

Unless this angle is near 90°, there will always be an element of over- or under-estimation. For non-radial tails, it is evident that the three-dimensional location of the observer with relation to the comet's tail will be a contributing factor towards the disparity between the measured and observed values. To truly test this technique, spacecraft observations with high temporal resolution of a comets ion tail with a near 90° orbit plane angle would help to remove geometrical perspective effects.

5.1.2 Amateur versus Professional Observations

Spacecraft data are consistently recorded with the same equipment and manner with little external influence on the way the data is processed and saved. Equally, sources of noise for the spacecraft instruments, commissioned by professional scientists, will be better constrained and more consistently removed from the data. Amateur observers are much less coordinated in this respect. They are limited by the consumer technology available and their individual budgets. This leads to a wide array of telescopes, detector types and FOVs being used to monitor the target, often without the use of any filters. There is no method of ensuring the equipment set up and data reduction are performed in a consistent manner. Though most amateur images of comets are likely to be calibrated, they will not be subjected to the same scientific rigour as observatory processing pipelines or spacecraft observations and may not have obtained all the necessary calibration frames. Furthermore, there tends to be an observational bias in the ion tail images gathered by amateur observers. Most of these images were acquired by volunteer astrophotographers and thus will publish their most aestheticically-pleasing and dynamic ion tail images. The timescales for the observations also differ. Spacecraft observations have delivered a high cadence of observations from the same instrument over a short period of time. Amateur astronomers tend to observe in short bursts over long periods of time. Inclement weather can often stymie consecutive observations leading to large data gaps in our resulting plots. Optical observations are prone to distortions. *Astrometry.net* calculates a Simple Imaging Polynomial (SIP) to represent image distortion (Shupe et al., 2005) of order 2, which is applied when mapping the photographs into their equatorial coordinates. Considering the maximum FOV astronomical images are a few degrees apart, with the comet often covering a subsection of that, the optical distortion should not cause a large discrepancy in the orbital plane mapping.

Knowing the accuracy of the image time is paramount to the success of our software. The unknown timing information played a larger role than had been initially anticipated in determining accurate v_{sw} estimates. The range of possible times for optocenters covering a large pixel area can lead to incorrect image projection. In such instances, the ion tail will appear closer or further from the solar radial vector leading to over/underestimations of the solar wind velocities. This is a likely strong source of the data scatter in our results. Whilst the amateur community is getting better at reporting this information, our professional-amateur collaboration would benefit immensely by organising mass requests of images and being specific about the information required including standardised metadata.

5.1.3 Turbulent events / Non-radial flows

Transient interplanetary events were partially responsible for deviations from the modelled solar wind velocities. Large radial velocities exceeding 1000 kms^{-1}, peaking at ∼1650 kms^{-1}, were recorded. Velocity vector maps of turbulent ionic features in consecutive images suggested that it was possible to at least constrain the velocity and expansion of the interaction region between ICMEs and the comet's ion tail. By comparing our image catalogue, our velocity estimates, MHD SW velocities and the CME catalogues, we can identify the list of likely transient phenomena. Some disturbances in the ion tail can often look like ICME-related turbulent events, appearing as a kink or a double ion tail, in certain instances. These could be due to the perspective viewing of a fast ion tail packet catching up with an earlier, slower moving condensation cloud.

6 Conclusions

We have demonstrated a new technique to extract v_{sw} estimates, as well as characterising general local parameters for transient interplanetary events near comets, allowing us to use comets as solar wind monitors throughout the inner heliosphere. The techniques demonstrated here rely heavily on high production rate comets that were close enough to the Sun to form a bright, observable ion tail. Nonetheless, the frequency of bright comets is significant enough to create a catalogue of solar wind velocities in the inner heliosphere. The big picture was to build a comprehensive view of the large scale and small scale variations throughout the inner heliosphere over past solar cycles.

Uncertainties in the solar wind velocities may arise from a number of identified and quantified error sources, chief amongst which are non-radial components of v_{sw}. Mapping the images onto the comet's orbital plane provides a good estimate of v_{sw_r} but the inherent uncertainties always need to be borne in mind. To summarise our caveats:

1. The core technique is the determination of multi-point, multi-latitudinal radial mass-loaded v_{sw} at the comet
2. Ground-based observations are at the mercy of the elements and there isnt much that amateur astrophotographers can do to minimise this effect on data quality.
3. It is unclear which amateur images have been calibrated and treated with due scientific rigour. This will only get better by improving collaborations between professional and amateur observers, and informing the amateur community of best practices for scientific analysis, inlcuding accurate and precise recording of the times at which images were obtained.
4. Our technique seems to be impeded by a recurring curving ion tail. It remains to be determined whether this is a characteristic of all comets or whether the technique will incorrectly underestimate solar wind velocities far from the nucleus and overestimate values close to the comet head.
5. infer general solar wind variations with solar cycle.
6. detection of transient events such as HCS crossings, CIR and ICME interactions

Our results of the global structure of the solar wind were mostly limited to the equatorial plane, which showed large spikes in v_{sw_r}. They do not always match the extrapolated near-Earth data or ENLIL MHD model perfectly. However, the close correlation during quiescent solar wind periods and the identified transient solar wind phenomena for most of the non-corresponding periods clearly show that the technique holds potential to diminish our knowledge gap of the solar wind variation in the inner heliosphere, as a complementary dataset to MHD models. The large error bars for the v_{sw_r} estimates arise either due to poor image quality, the plasma tail sampling technique or wide and diffuse plasma tails.

The results of this work do not entirely support our original hypothesis that amateur images of comets can be used as a reliable source for remote investigation of the solar wind. Though they can provide a rough indication of the bulk plasma flow velocity, though at times this is marred by the numerous heliospheric phenomena causing turbulence in the cometary ion tail. The observing geometry is an unexpectedly large factor in controlling the quality of the results. When applied to professional spaceborne observations, the technique yields comparable estimates of the v_{sw}. In stark contrast, the spacecraft data yielded a mostly smooth variation for the solar wind velocities. A high orbit plane angle of near 90° is considered to be the optimal observing scenario to produce high-quality, reliable estimates of the v_{sw}. In conclusion, v_{sw} estimates derived for amateur images are useful hints as to the solar wind behaviour as long as they are strictly considered under the caveats discussed previously.

6.1 Future work

The software and technique presented here is being been adapted to an online web service. Once fully operational, amateur observers will be able to contribute images for analysis. If successful, it could be beneficial to coordinate a select group of skilled amateur astrophotographers dispersed globally and equip them with a red and blue broadband filter at a minimum and ideally also with narrowband filters. Interesting to pursue would be to characterise the solar wind-geometrical dependency with a three dimensional triangulation of the plasma tail. This is achievable by comparing simultaneous observations of the ion tail from different vantage points. A similar study was done by Thompson (2009). They could only apply their technique to the dust tail as there were no stereoscopic observation of the ion tail until C/2011 W3 (Lovejoy) was observed. The technique could not be translated to the ion tail due to the complexity of the ion tails nonradial motion and the observers geometrical perspective. Another avenue worth investigating would be to identify the causal factor for the arcing nature of the ion tail. Simply determining whether the decreasing velocity trend downtail is a physical manifestation of the interaction between the mass-loaded solar wind and the charged dust tail, or whether it is an artefact of this technique, would be very informative.

Acknowledgments
This material is based upon work by YR supported by the National Aeronautics and Space Administration under Grant No. 80NSSC18K0971 issued through the SSO Near Earth Object Observations Program. Both authors are grateful to the UK Science and Technology Facilities Countil, Royal Astronomical Society, and the Daiwa Anglo-Japanese Foundation for funding during this work. YR also acknowledges the UK Institute of Physics for support. The excellent and very proactive community of amateur astronomers have helped make this project very interesting. Their willingness to contribute their data freely towards science has been near unanimous and we would like to thank them for making this research possible. This research made use of data processed through Astrometry.net. YR is grateful to Chris Arridge, Gethyn Lewis and Lin Gilbert for help with the programming. Wilcox Solar Observatory (currently supported by NASA) data used in this study was obtained via the web site http://wso.stanford.edu courtesy of J.T. Hoeksema. We extend our gratitude to the SOHO/LASCO and UK SECCHI science team at RAL for the data, advice and timely assistance and are grateful to R. Howard (NRL), PI of both the LASCO and SECCHI instruments. The CME catalogue employed is generated and maintained at the CDAW Data Center by NASA and The Catholic University of America in cooperation with the Naval Research Laboratory. We also used data from the CACTus CME catalogue, generated and maintained by the SIDC at the Royal Observatory of Belgium. Wilcox Solar Observatory data used in this study was obtained via the web site http://wso.stanford.edu courtesy of J.T. Hoeksema. The Wilcox Solar Observatory is currently supported by NASA. A critical aspect of this project would have been unfeasible without the training and data acquired during both INT discretionary times and our own proposal. Simulation results have been provided by the Community Coordinated Modeling Center at Goddard Space Flight Center through their public Runs on Request system (http://ccmc.gsfc.nasa.gov). The CCMC is a multi-agency partnership between NASA, AFMC, AFOSR, AFRL, AFWA, NOAA, NSF and ONR. The ENLIL Model was developed by Odstrcil, D. at University of Colorado at Boulder.

The processed data for the comets studied in this project and a description of the data can be found at: `https://doi.org/10.6084/m9.figshare.17197595.v4`, `https://doi.org/10.6084/m9.figshare.17197685.v1` and `https://doi.org/10.6084/m9.figshare.17197757.v1`.

References

Altschuler, M. D., & Newkirk, G. (1969, sep). Magnetic fields and the structure of the solar corona. *Solar Physics*, *9*(1), 131–149. Retrieved from `https://ui.adsabs.harvard.edu/abs/1969SoPh....9..131A/abstracthttp://link.springer.com/10.1007/BF00145734` doi: 10.1007/BF00145734

Belton, M. J. S., & Brandt, J. C. (1966, jun). Interplanetary Gas. XII. a Catalogue of Comet-Tail Orientations. *The Astrophysical Journal Supplement Series*, *13*, 125. Retrieved from `http://adsabs.harvard.edu/doi/10.1086/190138` doi: 10.1086/190138

Biermann, L. (1957). Solar corpuscular radiation and the interplanetary gas. *Obs*, *77*, 109–110.

Brandt, J., & Chapman, R. (2004). *Introduction to comets 2nd edition.* Retrieved 2021-03-24, from `https://www.cambridge.org/us/academic/subjects/physics/planetary-systems-and-astrobiology/introduction-comets-2nd-edition?format=PB&isbn=9780521004664`

Brandt, J. C. (1967, jan). Interplanetary Gas. XIII. Gross Plasma Velocities from the Orientations of Ionic Comet Tails. *The Astrophysical Journal*, *147*(9), 201. Retrieved from `http://adsabs.harvard.edu/doi/10.1086/148992` doi: 10.1086/148992

Brandt, J. C., Harrington, S. R., & Roosen, R. G. (1973, aug). Interplanetary Gas. XIX. Observational Evidence for a Meridional Solar-Wind Flow Diverging from the Plane of the Solar Equator. *The Astrophysical Journal*, *184*, 27–32. Retrieved from `https://ui.adsabs.harvard.edu/abs/1973ApJ...184...27B/abstract` doi: 10.1086/152299

Brandt, J. C., & Heise, J. (1970, mar). Interplanetary Gas. XV. Nonradial Plasma Motions from the Orientations of Ionic Comet Tails. *The Astrophysical Journal*, *159*, 1057. Retrieved from `https://ui.adsabs.harvard.edu/abs/1970ApJ...159.1057B/abstracthttp://adsabs.harvard.edu/doi/10.1086/150383` doi: 10.1086/150383

Brandt, J. C., Roosen, R. G., & Harrington, R. S. (1972, November). Interplanetary gas. XVII. an astrometric determination of solar wind velocities from orientations of ionic comet tails. *The Astrophysical Journal*, *177*, 277-284. doi: 10.1086/151706

Brandt, J. C., & Snow, M. (2000, November). Heliospheric Latitude Variations of Properties of Cometary Plasma Tails: A Test of the Ulysses Comet Watch Paradigm. *Icarus*, *148*, 52-64. doi: 10.1006/icar.2000.6484

Brueckner, G. E., Howard, R. A., Koomen, M. J., Korendyke, C. M., Michels, D. J., Moses, J. D., … Eyles, C. J. (1995, December). The Large Angle Spectroscopic Coronagraph (LASCO). *Solar Physics*, *162*, 357-402. doi: 10.1007/BF00733434

Buffington, A., Bisi, M. M., Clover, J. M., Hick, P. P., Jackson, B. V., & Kuchar, T. A. (2008, April). Analysis of Plasma-Tail Motions for Comets C/2001 Q4 (NEAT) and C/2002 T7 (LINEAR) Using Observations from SMEI. *The Astrophysical Journal*, *677*(1), 798-807. doi: 10.1086/529039

Combi, M. R., Bertaux, J.-L., Quémerais, E., Ferron, S., Mäkinen, J. T. T., & Aptekar, G. (2014, apr). WATER PRODUCTION IN COMETS C/2011 L4 (PanSTARRS) AND C/2012 F6 (LEMMON) FROM OBSERVATIONS WITH SOHO /SWAN. *The Astronomical Journal*, *147*(6), 126. Retrieved from `http://ssd.jpl.nasa.gov/horizons.cgi.https://iopscience.iop.org/article/10.1088/0004-6256/147/6/126` doi: 10.1088/0004-6256/147/6/126

Delva, M., Schwingenschuh, K., Niedner, M. B., & Gringauz, K. I. (1991). Comet Halley remote plasma tail observations and in situ solar wind properties: VEGA- 1 2 IMF/plasma observations and ground-based optical observations from 1 December 1985 to 1 May 1986. *Planetary and Space Science*, *39*(5), 697–708. doi: 10.1016/0032-0633(91)90063-G

Eyles, C. J., Harrison, R. A., Davis, C. J., Waltham, N. R., Shaughnessy, B. M., Mapson-Menard, H. C. A., … Rochus, P. (2009, feb). The Heliospheric Imagers Onboard the STEREO Mission. *Solar Physics*, *254*(2), 387–445. Retrieved from `https://ui.adsabs.harvard.edu/abs/2009SoPh..254..387E/abstracthttp://link.springer.com/10.1007/s11207-008-9299-0` doi: 10.1007/s11207-008-9299-0

Fulle, M., Leblanc, F., Harrison, R. A., Davis, C. J., Eyles, C. J., Halain, J. P., … Scarmato, T. (2007, may). Discovery of the Atomic Iron Tail of Comet MCNaught Using the Heliospheric Imager on STEREO. *The Astrophysical Journal*, *661*(1), L93–L96. Retrieved from `https://ui.adsabs.harvard.edu/abs/2007ApJ...661L..93F/abstracthttps://iopscience.iop.org/article/10.1086/518719` doi: 10.1086/518719

Giorgini, J. D., Yeomans, D. K., Chamberlin, A. B., Chodas, P. W., Jacobson, R. A., Keesey, M. S., … Wimberly, R. N. (1996, sep). JPL's On-Line Solar System Data Service. *American Astronomical Society*, *28*(25.04), 1158. Retrieved from `https://ui.adsabs.harvard.edu/abs/1996DPS....28.2504G/abstract`

Gopalswamy, N., Yashiro, S., Michalek, G., Stenborg, G., Vourlidas, A., Freeland, S., & Howard, R. (2009, apr). The SOHO/LASCO CME Catalog. *Earth, Moon, and Planets*, *104*(1-4), 295–313. doi: 10.1007/s11038-008-9282-7

Grison, B., Souček, J., Krupar, V., Píša, D., Santolík, O., Taubenschuss, U., & Němec, F. (2018, December). Shock deceleration in interplanetary coronal mass ejections (ICMEs) beyond Mercury's orbit until one AU. *Journal of Space Weather and Space Climate*, *8*, A54. doi: 10.1051/swsc/2018043

Hoeksema, J. T., Hoeksema, & Todd, J. (1991). Large-scale solar and heliospheric magnetic fields. In *Proceedings of symposium 9 of the 28th cospar plenary meeting* (Vol. 11, pp. 15–24). Retrieved from `https://ui.adsabs.harvard.edu/abs/1991AdSpR..11a..15H/abstract`

Hoffmeister, C. (1943). Physikalische Untersuchungen an Kometen. I. Die Beziehungen des primären Schweifstrahls zum Radiusvektor. Mit 2 Abbildungen. *Zeitschrift für Astrophysik*, *22*, 265.

Hogg, D. W., & Lang, D. (2008, dec). Astronomical imaging: The theory of everything. In *Aip conference proceedings* (Vol. 1082, pp. 331–338). AIP. Retrieved from `https://ui.adsabs.harvard.edu/abs/2008AIPC.1082..331H/abstracthttp://aip.scitation.org/doi/abs/10.1063/1.3059072` doi: 10.1063/1.3059072

Howard, R. A., Moses, J. D., Vourlidas, A., Newmark, J. S., Socker, D. G., Plunkett, S. P., … Carter, T. (2008, apr). Sun Earth Connection Coronal and Heliospheric Investigation (SECCHI). *Space Science Reviews*, *136*(1-4), 67–115. Retrieved from `https://ui.adsabs.harvard.edu/abs/2008SSRv..136...67H/abstracthttp://link.springer.com/10.1007/s11214-008-9341-4` doi: 10.1007/s11214-008-9341-4

Jian, L. K., MacNeice, P. J., Taktakishvili, A., Odstrcil, D., Jackson, B., Yu, H. S., … Evans, R. M. (2015, May). Validation for solar wind prediction at Earth: Comparison of coronal and heliospheric models installed at the CCMC. *Space Weather*, *13*(5), 316-338. doi: 10.1002/2015SW001174

Jockers, K. (1981, September). Plasma dynamics in the tail of Comet Kohoutek 1973 XII. *Icarus*, *47*(3), 397-411. doi: 10.1016/0019-1035(81)90188-3

Jockers, K. (1985, December). The ion tail of Comet Kohoutek 1973 XII during 17 days of solar wind gusts. *Astronomy and Astrophysics Supplement Series*, *62*, 791-838.

Jones, G. H. (2002, jun). The draping of heliospheric magnetic fields upstream of coronal mass ejecta. *Geophysical Research Letters*, *29*(11), 1520. doi: 10.1029/2001GL014110

Jones, G. H., & Brandt, J. C. (2004, October). The interaction of comet 153P/Ikeya-Zhang with interplanetary coronal mass ejections: Identification of fast ICME signatures. *Geophysics Research Letters*, *31*, L20805. doi: 10.1029/2004GL021166

Jones, G. H., Knight, M. M., Battams, K., Boice, D. C., Brown, J., Giordano, S., … McCauley, P. (2018, February). The Science of Sungrazers, Sunskirters, and Other Near-Sun Comets. *Space Science Reviews*, *214*(1), 20. doi: 10.1007/s11214-017-0446-5

Kaiser, M. (2005, jan). The STEREO mission: an overview. *Advances in Space Research*, *36*(8), 1483–1488. Retrieved from `https://ui.adsabs.harvard.edu/abs/2005AdSpR..36.1483K/abstracthttps://linkinghub.elsevier.com/retrieve/pii/S0273117705000505` doi: 10.1016/j.asr.2004.12.066

Konopleva, V. P., & Rozenbush, V. K. (1974). Perspective projection of cometary images on to the orbital plane. *Astrometriia i Astrofizika*, *22*, 61–69. Retrieved from `https://ui.adsabs.harvard.edu/abs/1974AAfz...22...61K/abstract`

Koutchmy, S., & Lamy, P. L. (1985). The F-Corona and the Circum-Solar Dust Evidences and Properties (ir). In R. H. Giese & P. Lamy (Eds.), *Iau colloq. 85: Properties and interactions of interplanetary dust* (p. 63). doi: 10.1007/978-94-009-5464-9_14

Lang, D., & Hogg, D. W. (2012, aug). Searching for Comets on the World Wide Web: The Orbit of 17P/Holmes from the Behavior of Photographers. *The Astronomical Journal*, *144*(2), 46. doi: 10.1088/0004-6256/144/2/46

Lang, D., Hogg, D. W., Mierle, K., Blanton, M., & Roweis, S. (2010, may). Astrometry.net: Blind Astrometric Calibration of Arbitrary Astronomical Images. *The Astronomical Journal*, *139*(5), 1782–1800. doi: 10.1088/0004-6256/139/5/1782

Minami, S., & White, R. S. (1986, aug). An acceleration mechanism for cometary plasma tails. *Geophysical Research Letters*, *13*(8), 849–852. Retrieved from `https://ui.adsabs.harvard.edu/abs/1986GeoRL..13..849M/abstracthttp://doi.wiley.com/10.1029/GL013i008p00849` doi: 10.1029/GL013i008p00849

Moore, E. P. (1991, jul). *Cometary ray closing rates - Comet Kobayashi-Berger-Milon* (Vol. 247; Tech. Rep. No. 1). Retrieved from `https://ui.adsabs.harvard.edu/abs/1991A%26A...247..247M/abstract`

Morrill, J. S., Korendyke, C. M., Brueckner, G. E., Giovane, F., Howard, R. A., Koomen, M., … Andrews, M. (2006, feb). Calibration of the Soho/Lasco C3 White Light Coronagraph. *Solar Physics*, *233*(2). Retrieved from `https://ui.adsabs.harvard.edu/abs/2006SoPh..233..331M/abstracthttp://link.springer.com/10.1007/s11207-006-2058-1`

Niedner, M. B., Jr., & Brandt, J. C. (1978, July). Interplanetary gas. XXII - Plasma tail disconnection events in comets - Evidence for magnetic field line reconnection at interplanetary sector boundaries. *The Astrophysical Journal*, *223*, 655-670. doi: 10.1086/156299

Owens, M., & Cargill, P. (2004, dec). Non-radial solar wind flows induced by the motion of interplanetary coronal mass ejections. *Annales Geophysicae*, *22*(12), 4397–4406. doi: 10.5194/angeo-22-4397-2004

Ramanjooloo, Y. (2015, oct). Comets as natural laboratories: Interpretations of the structure of the inner heliosphere. *Doctoral thesis, UCL (University College London)..* Retrieved from `https://discovery.ucl.ac.uk/id/eprint/1471003/`

Ramanjooloo, Y., & Jones, G. H. (2021a). *Radial and Non-Radial Solar wind velocities for C/2011 L4 (PANSTARRS) (Version 1) [Dataset].* figshare. doi: https://doi.org/10.6084/m9.figshare.17197757.v1

Ramanjooloo, Y., & Jones, G. H. (2021b). *Solar wind velocities for C/2013 R1*

(Lovejoy) (Version 4) [Dataset]. figshare. doi: https://doi.org/10.6084/m9.figshare.17197595.v4

Ramanjooloo, Y., & Jones, G. H. (2021c). *Solar wind velocities for comet C/2013 R1 (Lovejoy) during low orbit plane angles (Version 1) [Dataset].* figshare. doi: https://doi.org/10.6084/m9.figshare.17197685.v1

Raouafi, N.-E., Lisse, C. M., Stenborg, G., Jones, G. H., & Schmidt, C. A. (2015, jul). Dynamics of HVECs emitted from comet C/2011 L4 as observed by STEREO. *Journal of Geophysical Research: Space Physics*, *120*(7), 5329–5340. Retrieved from `http://doi.wiley.com/10.1002/2014JA020926` doi: 10.1002/2014JA020926

Rauer, H., & Jockers, K. (1990). *Focal Reducer Observations of Comets Liller 1988a and P/Tempel 2 1987g* (Tech. Rep.). Retrieved from `https://ui.adsabs.harvard.edu/abs/1990acm..proc..417R/abstract`

Richardson, J. D., Belcher, J. W., Lazarus, A. J., Paularena, K. I., Steinberg, J. T., & Gazis, P. R. (1996, may). Non-radial flows in the solar wind. In *Aip conference proceedings* (Vol. 382, pp. 479–482). AIP. doi: 10.1063/1.51432

Schatten, K. H., Wilcox, J. M., & Ness, N. F. (1969, mar). A model of interplanetary and coronal magnetic fields. *Solar Physics*, *6*(3), 442–455. Retrieved from `https://ui.adsabs.harvard.edu/abs/1969SoPh....6..442S/abstracthttp://link.springer.com/10.1007/BF00146478` doi: 10.1007/BF00146478

Schlosser, W. (1967). *Photographic Structures Within Comet Morehouse 1908 III* (Vol. 13; Tech. Rep.). Retrieved from `https://ui.adsabs.harvard.edu/abs/1967LIACo..13..343S/abstract`

Shupe, D. L., Moshir, M., Li, J., Makovoz, D., Narron, R., & Hook, R. N. (2005, December). The SIP Convention for Representing Distortion in FITS Image Headers. In P. Shopbell, M. Britton, & R. Ebert (Eds.), *Astronomical data analysis software and systems xiv* (Vol. 347, p. 491).

Sizonenko, Y. V. (2007). Comets C/2001 Q4 and C/2004 Q2: Structure of plasma tails. *Kinematics and Physics of Celestial Bodies*, *23*(5), 207–213. doi: 10.3103/s0884591307050042

Thompson, W. T. (2009). 3D triangulation of a Sun-grazing comet. *Icarus*, *200*(2), 351–357. doi: 10.1016/j.icarus.2008.12.011

Vourlidas, A., Davis, C. J., Eyles, C. J., Crothers, S. R., Harrison, R. A., Howard, R. A., ... Socker, D. G. (2007, October). First Direct Observation of the Interaction between a Comet and a Coronal Mass Ejection Leading to a Complete Plasma Tail Disconnection. *The Astrophysical Journal*, *668*, L79-L82. doi: 10.1086/522587

Wainscoat, R., Micheli, M., Wells, L., Holmes, R., Foglia, S., Vorobjov, T., ... Williams, G. V. (2011, jun). Comet C/2011 L4 (Panstarrs). *IAU Circ.*, *9215*, 1. Retrieved from `https://ui.adsabs.harvard.edu/abs/2011IAUC.9215....1W/abstract`

Watanabe, J. I. (1991, apr). Measurement of the solar wind velocity with cometary tail rays. *Solar Physics*, *132*(2), 395–407. Retrieved from `https://ui.adsabs.harvard.edu/abs/1991SoPh..132..395W/abstract` doi: 10.1007/BF00152295

Wilson, J. K., Baumgardner, J., & Mendillo, M. (1998, feb). Three tails of comet Hale-Bopp. *Geophysical Research Letters*, *25*(3), 225–228. Retrieved from `http://doi.wiley.com/10.1029/97GL03704` doi: 10.1029/97GL03704

Yagi, M., Koda, J., Furusho, R., Terai, T., Fujiwara, H., & Watanabe, J.-I. (2015, feb). Initial Speed of Knots in the Plasma Tail of C/2013 R1 (LOVEJOY) INITIAL SPEED OF KNOTS IN THE PLASMA TAIL OF C/2013 R1(LOVEJOYINITIAL SPEED OF KNOTS IN THE PLASMA TAIL OF C/2013 R1(LOVEJOY). *The Astronomical Journal*, *149*(3), 97. Retrieved from `https://iopscience.iop.org/article/10.1088/0004-6256/149/3/97`

doi: 10.1088/0004-6256/149/3/97
York, D. G., Adelman, J., Anderson, J., John E., Anderson, S. F., Annis, J., Bahcall, N. A., ... SDSS Collaboration (2000, September). The Sloan Digital Sky Survey: Technical Summary. *Astronomical Journal*, *120*(3), 1579-1587. doi: 10.1086/301513